Assessment of aeroacoustic resolution properties of DG schemes and comparison with DRP schemes

Ziqiang Cheng[1], Jinwei Fang,[2] Chi-Wang Shu[3] and Mengping Zhang[4]

Abstract

We discuss the aeroacoustic resolution properties of the discontinuous Galerkin (DG) schemes in detail and compare their performance with the state of the art finite difference (FD) schemes, including the classical dispersion-relation-preserving (DRP) schemes. Analysis shows that, even though the DG schemes are slightly dissipative, their overall dispersion and dissipation properties are comparable with the corresponding DRP schemes on the same stencil. For the convenience of a direct comparison with FD schemes, we write the DG schemes in the form of block finite difference schemes. Ample numerical tests, including the tests on nozzle flow problems, are performed and we observe that the DG schemes and DRP schemes with the same stencil produce comparable numerical results. Since the DG schemes are flexible on non-uniform meshes and general unstructured meshes, they should be good candidates for computational aeroacoustics, especially those on complex geometry.

Key Words: computational aeroacoustics, aeroacoustic resolution properties; DG schemes; DRP schemes

[1]School of Mathematical Sciences, University of Science and Technology of China, Hefei, Anhui 230026, P.R. China. E-mail: czq10491@mail.ustc.edu.cn

[2]School of Applied Mathematics, Guangdong University of Technology, Guangzhou 510006, Guangdong, P.R. China. Email: fangjinwei@gdut.edu.cn

[3]Division of Applied Mathematics, Brown University, Providence, RI 02912, USA. E-mail: shu@dam.brown.edu. Research supported by NSF grant DMS-1719410.

[4]School of Mathematical Sciences, University of Science and Technology of China, Hefei, Anhui 230026, P.R. China. E-mail: mpzhang@ustc.edu.cn. Research supported by NSFC grant 11871448.

1 Introduction

Computational aeroacoustics (CAA), a relatively young research area, is an interdisciplinary subject involving fluid mechanics, acoustics, computational geometry, numerical analysis, computer science and mathematical theory of partial differential equations. It not only uses numerical methods to study the mechanism of noise caused by flow and its interaction with objects, but also uses these methods to study practical engineering problems in aeroacoustics, providing a tool to control and reduce aeroacoustic noise. Due to the special features of acoustic problems, CAA requires, in some sense, much higher standard for numerical algorithms than the general computational fluid dynamics (CFD) does. The main challenges CAA faces are as follows. (1) Since the frequencies of aeroacoustic problems usually fall within a wide range, successful simulation of high frequency waves with short wavelengths is important. (2) The amplitude of the aeroacoustic fluctuation is very small. Compared with the mainstream energy in the flow field, it is usually smaller by 3-5 orders of magnitude. The numerical error can easily conceal the aeroacoustic fluctuation. Therefore, numerical schemes must have a small numerical error in order to accurately calculate the aeroacoustic characteristics. (3) In CAA, we are often interested in sound waves radiated far away. The numerical scheme should have good dispersion and dissipation properties, so that it has better accuracy over a long distance. (4) Artificial truncated boundary is formed in the process of truncating infinite domain into finite domain in numerical calculation. It is necessary to construct boundary conditions which allow all pulses to exit smoothly. Due to so many challenges, it is not easy to design good numerical methods for CAA problems.

One class of the most widely used and successful methods in CAA is Tam's dispersion-relation-preserving (DRP) scheme, which was first presented by Tam and Webb in [36]. These schemes select the difference coefficients by minimizing an integral error E, resulting in better propagation properties than the traditional difference schemes on the same stencils in both theoretical analysis (for linear hyperbolic equations) and many nu-

merical experiments. Tam also developed DRP schemes to compute nonlinear acoustic pulses [35] and studied non-reflecting boundary conditions [36] and short wave components in computational acoustics [37]. According to these studies, it is necessary to add artificial selective damping (ASD) terms to the numerical scheme when the error caused by short waves seriously pollutes the computed solution. Based on the idea of dispersion preservation, a large number of high resolution numerical schemes have been proposed by many researchers [2,6,16,18,24]. We could mention, in particular, optimized compact finite difference schemes proposed by Kim and Lee [22,23], optimized upwind dispersion-relation-preserving schemes proposed by Zhuang and Chen [42, 43], and low dissipation and low dispersion explicit schemes proposed by Bogey and Bailly [5]. However, most of these methods are based on the finite difference framework, making them less flexible for non-uniform and especially unstructured meshes.

The discontinuous Galerkin (DG) methods are a class of finite element methods using discontinuous piecewise polynomials as basis functions and test functions. It was first developed by Reed and Hill [26] in 1973 to study steady-state linear neutron transport, and significant progress was made by Cockburn et al in a series of work [7, 8, 10, 11] for numerically solving hyperbolic conservation laws. Discontinuous Galerkin methods have many advantages, such as high order accuracy, flexibility in h-p adaptivity, high parallel efficiency, and flexibility for arbitrary geometry and meshes, which make DG very popular in many applications.

For wave propagations, work has been done in the literature to analyze the dispersion and dissipation behavior of DG schemes. Sherwin [27] analyzed the dispersion and dissipation relation of the semi-discrete continuous and discontinuous Galerkin formulations for the linear advection equation and found that the discontinuous Galerkin scheme is more diffusive. Zhong and Shu [40] made a quantitative error analysis and superconvergence analysis of the semi-discrete DG scheme for the linear convection equation. For the fully discrete scheme, the number of points needed for each wavelength to obtain a

specific error was computed. Guo et al [14] used Fourier method to analyze the error properties of DG and LDG methods and observed that the error can be divided into three parts. Ainsworth [1] studied dispersive properties of the h-p version discontinuous Galerkin schemes in three different limits and gave the decay behavior of the dispersion and dissipation errors of DG schemes in each case. Hu et al [20] investigated dispersion and dissipation properties of the discontinuous Galerkin method designed on triangular and rectangular meshes for one and two dimensional advection equations. Hu and Atkins [19] extended this analysis to non-uniform grids and to systems of linear hyperbolic equations. However, a detailed evaluation of the propagation properties of DG schemes, when compared with other state of the art schemes in CAA, seems to be still missing. In this paper, we fill this gap and present a simple method to analyze the propagation properties of DG schemes for linear convection equation in detail, including the dispersion properties of physical and virtual waves, the dissipative properties and the relationship between the two waves and initial values. By comparing the dispersion properties of the DG schemes with those of various finite difference (FD) schemes, including the DRP schemes, we find the excellent performance of DG schemes in simulating wave propagation, comparable with the state of the art DRP schemes on the same stencils.

In addition, we also study the performance of DG schemes on classical CAA problems, following earlier work in the literature, including Atkins and Shu [4] which applied a quadrature-free form of the DG method to solve the linear Euler equations prescribed as part of the ICASE/LaRC Workshop [17] on Benchmark Problems in Computational Aeroacoustics. Atkins [3] studied on how to reasonably select boundary conditions when applying DG schemes to CAA problems in detail. Here, we apply DG schemes to a series of standard 1D test problems and the nozzle flow. By comparing different DG schemes and finite difference schemes, it is shown that the DG schemes are compatible (sometimes better, sometimes a bit worse) with DRP schemes using the same number of degrees of freedom per wave, for standard 1D test problems and for the nozzle problem.

We mainly focus on linear problems, but also consider some nonlinear cases. Since the DG schemes are flexible on non-uniform meshes and general unstructured meshes, they should be good candidates for CAA problems, especially those on complex geometry.

The remainder of this paper is organized as follows. In section 2, we introduce and analyze the dispersion properties of DG schemes for linear scalar equation in detail and take the P^1 element as an example to show the main ideas. In section 3, we compare the dispersion properties of different schemes and write the DG schemes in the form of block finite difference schemes for easier comparison with other finite difference schemes. Section 4 studies group velocities, and section 5 briefly discusses numerical stability. In section 6, a series of numerical examples are presented to demonstrate the performance of DG schemes and the comparison with other FD schemes. Finally, concluding remarks are given in section 7.

2 Dispersion properties of the discontinuous Galerkin method

Following the idea of Fourier analysis in [15], we consider the following linear advection equation:

$$u_t + u_x = 0 \tag{2.1a}$$

$$u(x,0) = e^{ikx} \tag{2.1b}$$

The exact solution is given by $u(x,t) = e^{i(kx-\omega t)}$ with $\omega = k$. This is the physical dispersion relation. Now we would like to find a numerical dispersion relation for the discontinuous Galerkin (DG) method. We first define the following mesh and finite element space:

$$x_j = \left(j - \frac{1}{2}\right) h, \quad I_j = [x_{j-1/2}, x_{j+1/2}], \quad V_h^q = \{v : v|_{I_j} \in \mathscr{D}^q(I_j)\}$$

where $\mathscr{D}^q$ denotes the space of polynomials of degree at most q. Using the L^2 projection of the initial condition on V_h^q as the initial value of the DG solution, the semi-discrete

DG scheme is: find the unique function $u_h = u_h(t) \in V_h^q$, such that for all test functions $v_h \in V_h^q$ and all j, the following equations hold:

$$\int_{I_j} (u_h)_t v_h dx = \int_{I_j} u_h (v_h)_x dx - \hat{u}_{j+1/2}(v_h)^-_{j+1/2} + \hat{u}_{j-1/2}(v_h)^+_{j-1/2} \tag{2.2a}$$

$$u_h(x,0) = P(e^{ikx}) \tag{2.2b}$$

Here, the upwind numerical flux is given by $\hat{u}_{j\pm1/2} = u_h(x^-_{j\pm1/2})$, and $(v_h)^\pm_{j+1/2} = v_h(x^\pm_{j+1/2})$. $P(e^{ikx})$ is the L^2 projection of e^{ikx} in V_h^q, i.e.

$$P(e^{ikx}) \in V_h^q, \qquad \int_{I_j} (e^{ikx} - P(e^{ikx}))v(x) = 0, \text{ for all } j \text{ and } v(x) \in V_h^q \tag{2.3}$$

We assume that the solution of (2.2a) is $u_h(x,t)|_{I_j} = \sum_{m=0}^q u_m^j(t)\varphi_m^j(x)$, where $\varphi_m^j(x)$, $m = 0, 1, \cdots, q$ are the Legendre polynomials on I_j. As an ansatz, $u_m^j(t)$ is taken as:

$$u_m^j(t) = e^{i(kx_j - \bar{\omega}t)}\beta_m \tag{2.4}$$

Substitute it into (2.2a), take v_h as $\varphi_l^j(x)$ and sort it out, we get:

$$\bar{\omega}\beta_l = \frac{i(2l+1)}{h} \sum_{m=0}^{q} \left(\int_{-1}^{1} \varphi_m \varphi_l' d\xi - 1 + e^{-ikh}(-1)^l \right) \beta_m \tag{2.5}$$

Here, $\varphi_l(\xi)$, $l = 0, 1, \cdots, q$ are the Legendre polynomials on $[-1, 1]$. $\varphi_l(-1) = (-1)^l$, $\varphi_l(1) = 1$ are used in the equations above. We denote $\boldsymbol{\beta} = (\beta_0, \beta_1, \cdots, \beta_q)^T$, $c_{lm} = \frac{i(2l+1)}{h}(\int_{-1}^{1} \varphi_m \varphi_l' d\xi - 1 + e^{-ikh}(-1)^l)$, $\boldsymbol{A} = (a_{ij})_{(q+1)\times(q+1)}$, $a_{ij} = c_{i-1,j-1}$. In the following discussion, we assume that $\boldsymbol{A}$ always has a complete set of eigenvectors. Equation (2.5) can be written as:

$$\boldsymbol{A}\boldsymbol{\beta} = \bar{\omega}\boldsymbol{\beta} \tag{2.6}$$

If $\bar{\omega}$ is an eigenvalue of $\boldsymbol{A}$ and $\boldsymbol{\beta}$ is its corresponding eigenvector, $u_h(x,t) = \sum_{m=0}^q u_m^j(t)$ $\varphi_m^j(x)$ is a "characteristic solution" of (2.2a). Since $\boldsymbol{A}$ has a complete set of eigenvectors, (2.2a) has $q+1$ linearly independent characteristic solutions. We write them down as $u_h^n(x,t) = \sum_{m=0}^q e^{i(kx_j - \bar{\omega}_n t)}\beta_{mn}\varphi_m^j(x), n = 0, 1, \cdots, q$. Now let us take the initial conditions into account and assume that the solution of the DG scheme (2.2) is interpreted

as:

$$u_h(x,t) = \sum_{n=0}^{q} \gamma_n u_h^n(x,t) = \sum_{m=0}^{q}\sum_{n=0}^{q} \gamma_n \beta_{mn} e^{i(kx_j - \bar{\omega}_n t)} \varphi_m^j(x) \tag{2.7}$$

Noting that

$$u_m^j(0) = \frac{\int_{I_j} \varphi_m^j(x) e^{ikx} dx}{\int_{I_j} (\varphi_m^j(x))^2 dx} = e^{ikx_j} \alpha_m, \tag{2.8}$$

where $\alpha_m = \frac{2m+1}{2} \int_{-1}^{1} \varphi_m(\xi) e^{ikh\xi/2} d\xi$, we would get:

$$\alpha_m = \sum_{n=0}^{q} \gamma_n \beta_{mn} \tag{2.9}$$

We denote $\boldsymbol{B} = (b_{ij})_{(q+1)\times(q+1)}$, $\boldsymbol{\gamma} = (\gamma_0, \gamma_1, \cdots, \gamma_q)^T$, $\boldsymbol{\alpha} = (\alpha_0, \alpha_1, \cdots, \alpha_q)^T$, where $b_{ij} = \beta_{i-1,j-1}$, then

$$\boldsymbol{B}\boldsymbol{\gamma} = \boldsymbol{\alpha} \tag{2.10}$$

Considering that $\boldsymbol{A}$ has a complete set of eigenvectors, $\boldsymbol{B}$ is invertible. We would obtain $\boldsymbol{\gamma} = \boldsymbol{B}^{-1}\boldsymbol{\alpha}$. By this time, the solution of equation (2.2) has been obtained completely. In order to analyze the propagation properties of the DG scheme, we denote $\bar{\omega}_n = \bar{\omega}_{nr} + i\bar{\omega}_{ni}$ and obtain

$$u_h(x,0) = \sum_{n=0}^{q} \gamma_n u_h^n(x,0) \tag{2.11}$$

$$\begin{aligned} u_h(x,t) &= \sum_{n=0}^{q} \gamma_n u_h^n(x,t) = \sum_{n=0}^{q} \gamma_n e^{\bar{\omega}_{ni} t} e^{-i\bar{\omega}_{nr} t} \sum_{m=0}^{q} e^{ikx_j} \beta_{mn} \varphi_m^j(x) \\ &= \sum_{n=0}^{q} e^{\bar{\omega}_{ni} t} e^{-i\bar{\omega}_{nr} t} \gamma_n u_h^n(x,0) \end{aligned} \tag{2.12}$$

We see that, the waveforms of the initial solution are superposed by $q+1$ waves, which propagate in accordance with $q+1$ different properties. $\bar{\omega}_{ni}$ and $\bar{\omega}_{nr}$ determine the dissipative and dispersive properties of their propagations respectively. If $\bar{\omega}_{ni} > 0$, the scheme is unstable; if $\bar{\omega}_{ni} < 0$, then the n-th wave has dissipation. The propagation speed of the n-th wave is $\bar{\omega}_{nr}/k$. After a detailed analysis of several different DG schemes, we could see that the dispersion relation of only one wave among all $q+1$ waves is consistent with that of the analytic solution when kh is relatively small. This wave is called the

physical wave while the other waves are called virtual waves. Without loss of generality, we assume that $\bar{\omega}_0$ stands for the propagation properties of the physical wave. $u_h(x,t)$ can be written as:

$$\begin{aligned} u_h(x,t) &= \gamma_0 u_h^0(x,0)e^{-i\bar{\omega}_{0r}t}e^{\bar{\omega}_{0i}t} + \sum_{n=1}^{q}\gamma_n u_h^n(x,0)e^{-i\bar{\omega}_{nr}t}e^{\bar{\omega}_{ni}t} \\ &= e^{-\frac{ikh\eta}{2}}\sum_{m=0}^{q}\beta_{m0}\varphi_m(\eta)e^{ikx}e^{-i\bar{\omega}_{0r}t}e^{\bar{\omega}_{0i}t} + \sum_{n=1}^{q}\gamma_n u_h^n(x,0)e^{-i\bar{\omega}_{nr}t}e^{\bar{\omega}_{ni}t} \\ &= r(\eta)e^{i\theta(\eta)}e^{ikx}e^{-i\bar{\omega}_{0r}t}e^{\bar{\omega}_{0i}t} + \sum_{n=1}^{q}\gamma_n u_h^n(x,0)e^{-i\bar{\omega}_{nr}t}e^{\bar{\omega}_{ni}t} \end{aligned}$$

Here, we assume that $x \in I_j$, and $\eta = \frac{2(x-x_j)}{h}$. $r(\eta) = |\sum_{m=0}^{q}\beta_{m0}\varphi_m(\eta)|$, $\theta(\eta) = \arg(\sum_{m=0}^{q}\beta_{m0}\varphi_m(\eta)) - kh\eta/2$. $r(\eta)e^{i\theta(\eta)}$ is the "initial physical wave proportion". For FD schemes, it is equal to 1. But for DG schemes, it is not. This phenomenon is caused by the initial conditions using the L^2 projection of the exact initial condition, and only physical waves propagating according to the correct properties. In order for the DG solutions to be reliable, the following three conditions must be satisfied:

- The initial physical wave proportion is very close to 1.
- The propagation property of the physical wave is very close to that of the exact solution.
- The dissipation of the virtual waves is very strong.

As an example, let us consider the piecewise linear case of $q = 1$. In this case, we can compute explicitly $\boldsymbol{A}$, $\boldsymbol{\alpha}$, $\bar{\boldsymbol{\omega}}$ as follows:

$$\boldsymbol{A} = \frac{i}{h}\begin{bmatrix} -1+e^{-ikh} & -1+e^{-ikh} \\ 3-3e^{-ikh} & -3-3e^{-ikh} \end{bmatrix}$$

$$\boldsymbol{\alpha} = \begin{cases} \left(\dfrac{2\sin(kh/2)}{hk}, -\dfrac{6i\left(hk\cos(kh/2) - 2\sin(kh/2)\right)}{h^2k^2}\right)^T, & kh \neq 0 \\ (1,0)^T \quad kh = 0 \end{cases}$$

$$\bar{\boldsymbol{\omega}} = \frac{1}{h}\begin{pmatrix} -ie^{-ikh}\left(-i\sqrt{-10e^{ikh}+2e^{2ikh}-1}+2e^{ikh}+1\right) \\ e^{-ikh}\left(\sqrt{-10e^{ikh}+2e^{2ikh}-1}-2ie^{ikh}-i\right) \end{pmatrix}$$

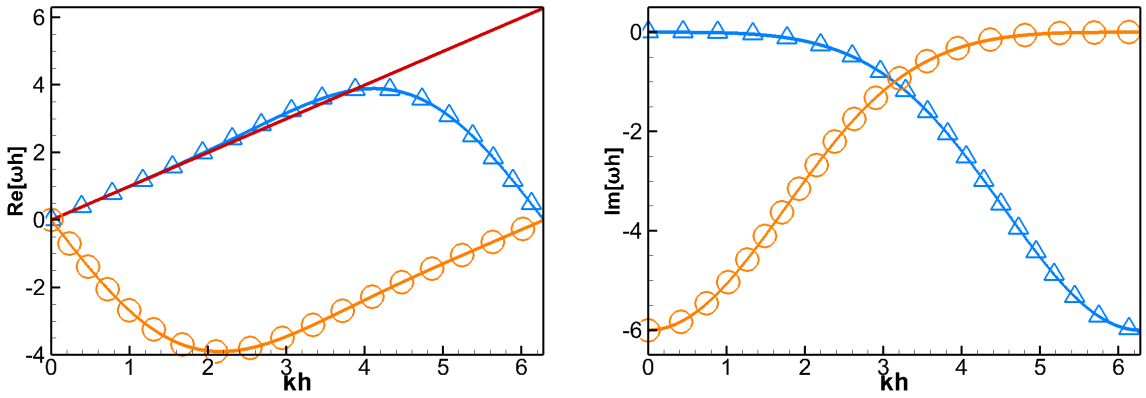

(a) Dispersion relation (b) Dissipation coefficient

Fig. 2.1. Exact dispersion, dispersion relation and the dissipation coefficient for the DG-P^1 scheme. Lines with delta symbols correspond to the physical waves, lines with circle symbols correspond to the virtual waves, and the solid line without any symbols represents the exact dispersion relation.

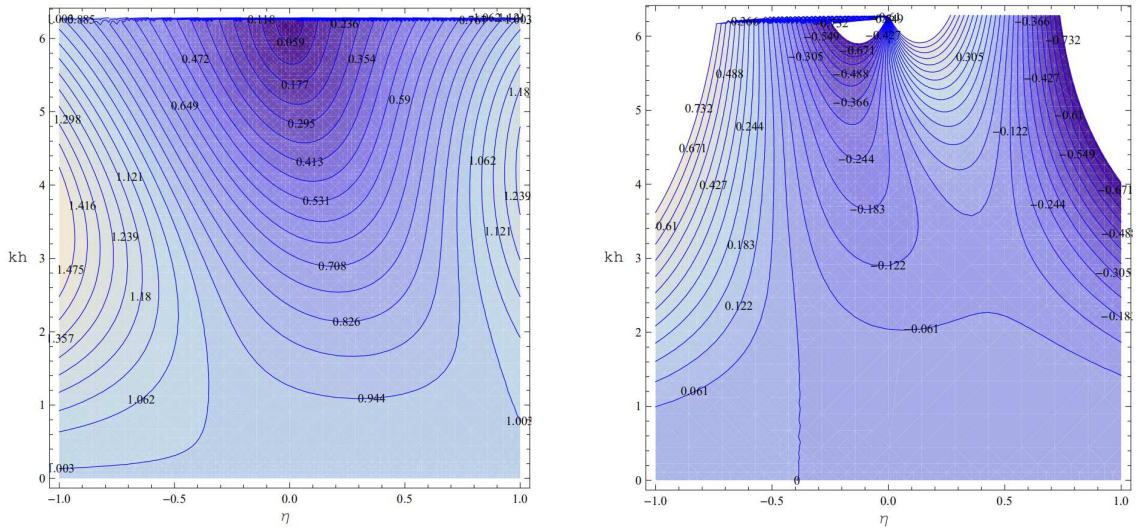

(a) Contour map of $r(\eta)$ (b) Contour map of $\theta(\eta)$

Fig. 2.2. The contour maps of modulus and principal argument angle of the initial physical wave proportion for the DG-P^1 scheme.

Then we can compute $\boldsymbol{B}$, $\boldsymbol{\gamma}$, $r(\eta)$, $\theta(\eta)$ and make relevant figures. Figure 2.1 shows the dispersion and dissipation properties of the physical and virtual waves for the DG-P^1 scheme. Figure 2.2 shows the distributions of modulus and principal argument angle of the initial physical wave proportion. It can be seen from the figure that when kh is small, the dispersion relation of the physical wave is very close to the exact dispersion relation, and the dissipation is very small; the virtual wave, of which the propagation direction is opposite to that of the exact solution, has strong dissipation; the initial physical wave proportion is close to 1. With the increase of kh, the dispersion relation of the physical wave begins to depart from the exact dispersion relation and the dissipation becomes stronger; the dissipation of the virtual wave becomes weaker; the initial physical wave proportion begins to depart from 1.

3 Comparison of dispersion relations among DG schemes, FD schemes and the DRP scheme

In addition to the DG scheme, we also consider the following commonly used numerical schemes for (2.1):

- 2nd-order central difference scheme (3-point scheme):

$$\frac{d}{dt}u_j + \frac{1}{h}\left(\frac{1}{2}u_{j+1} - \frac{1}{2}u_{j-1}\right) = 0 \tag{3.1}$$

- 4th-order central difference scheme (5-point scheme):

$$\frac{d}{dt}u_j + \frac{1}{h}\left(-\frac{1}{12}(u_{j+2} - u_{j-2}) + \frac{2}{3}(u_{j+1} - u_{j-1})\right) = 0 \tag{3.2}$$

- 6th-order central difference scheme (7-point scheme):

$$\frac{d}{dt}u_j + \frac{1}{h}\left(\frac{1}{60}(u_{j+3} - u_{j-3}) - \frac{3}{20}(u_{j+2} - u_{j-2}) + \frac{3}{4}(u_{j+1} - u_{j-1})\right) = 0 \tag{3.3}$$

- optimized 7-point DRP scheme [36] (7-point scheme):

$$\frac{d}{dt}u_j + \frac{1}{h}\left(a_3(u_{j+3} - u_{j-3}) + a_2(u_{j+2} - u_{j-2}) + a_1(u_{j+1} - u_{j-1})\right) = 0 \tag{3.4}$$

with

$$a_1 = 0.770882380518, \quad a_2 = -0.1667059044145, \quad a_3 = 0.020843142770$$

where u_j represents the approximation of u at $x_j = jh$. Scheme (3.4), the optimized 7-point DRP scheme, might be the most classical DRP scheme. In the following, when we mention the DRP scheme without further clarification, it will be referring to the scheme (3.4). For better intuition, we rewrite the formulations of the DG schemes as block finite difference (FD) schemes according to the idea in [39]. For DG-P^q, we take $I_j = [x_{j-q-1}, x_j]$ for $j \equiv 0 \,(\mathrm{mod}(q+1))$ as the DG cells, where $x_i = ih$ (that is, the DG cells are of the size $(q+1)h$), and we choose the following Lagrange basis functions:

$$\phi_{j-r}(x) = \frac{(x - x_{j-q})(x - x_{j-q+1}) \cdots (x - x_j)}{(x_{j-r} - x_{j-q})(x - x_{j-q+1}) \cdots (x_{j-r} - x_j)}, \quad r = 0, 1 \cdots, q \tag{3.5}$$

as the basis functions of the DG scheme. This choice of basis functions corresponds to the choice of point values at uniformly distributed points inside each cell including the right boundary but excluding the left boundary. Considering the upwind numerical flux, the definition of point values are given as $u_i = u_h(x_i^-)$. Here, the left limit is relevant only when $x_i = x_j$ with $j \equiv 0 \,(\mathrm{mod}(q+1))$, that is, when x_i is a boundary point of a cell. The DG scheme is then given as

$$\begin{aligned}\int_{I_j} \sum_{l=0}^{q} \phi_{j-l}\phi_{j-m}(u_{j-l})_t dx = \int_{I_j} \sum_{l=0}^{q} \phi_{j-l}\phi'_{j-m}u_{j-l}dx - \phi_{j-m}(x_j)u_j \\ + \phi_{j-m}(x_{j-q-1})u_{j-q-1}, \quad m = 0, 1, \cdots, q\end{aligned} \tag{3.6}$$

We denote

$$\boldsymbol{A}_j = (a_{rs}^{(j)})_{(q+1)\times(q+1)}, \quad \boldsymbol{B}_j = (b_{rs}^{(j)})_{(q+1)\times(q+1)}$$

$$\boldsymbol{U}_j = (u_{j-q}, u_{j-q+1}, \cdots, u_j)^T, \quad \boldsymbol{V}_j = (0, 0, 0, \cdots, -u_j)^T$$

$$\boldsymbol{W}_j = (\phi_{j-q}(x_{j-q-1})u_{j-q-1}, \phi_{j-q+1}(x_{j-q-1})u_{j-q-1}, \cdots, \phi_j(x_{j-q-1})u_{j-q-1})^T$$

where $a_{rs}^{(j)} = \int_{I_j} \phi_{j-q+r-1}\phi_{j-q+s-1}dx$, $b_{rs}^{(j)} = \int_{I_j} \phi'_{j-q+r-1}\phi_{j-q+s-1}dx$. Then (3.6) can be written as:

$$\boldsymbol{A}_j(\boldsymbol{U}_j)_t = \boldsymbol{B}_j\boldsymbol{U}_j + \boldsymbol{V}_j + \boldsymbol{W}_j \tag{3.7}$$

It can be easily verified that the mass matrix $\boldsymbol{A}_j$ is nonsingular. Then we get $(\boldsymbol{U}_j)_t = \boldsymbol{A}_j^{-1}\boldsymbol{B}_j\boldsymbol{U}_j + \boldsymbol{A}_j^{-1}\boldsymbol{V}_j + \boldsymbol{A}_j^{-1}\boldsymbol{W}_j$. The FD forms of DG-$P^1$ to P^5 are listed as follows.

- DG-P^1 (3-point scheme):

$$\frac{d}{dt}u_j = \begin{cases} \dfrac{1}{h}\left(\dfrac{1}{2}u_{j-1} - \dfrac{1}{2}u_{j+1}\right), & j \equiv 1\,(\mathrm{mod}2) \\ \dfrac{1}{h}\left(-u_{j-2} + 3u_{j-1} - 2u_j\right), & j \equiv 0\,(\mathrm{mod}2) \end{cases} \tag{3.8}$$

- DG-P^2 (4-point scheme):

$$\frac{d}{dt}u_j = \begin{cases} \dfrac{1}{h}\left(\dfrac{1}{9}u_{j-1} + \dfrac{7}{6}u_j - \dfrac{5}{3}u_{j+1} + \dfrac{7}{18}u_{j+2}\right), & j \equiv 1\,(\mathrm{mod}3) \\ \dfrac{1}{h}\left(-\dfrac{5}{9}u_{j-2} + \dfrac{13}{6}u_{j-1} - \dfrac{5}{3}u_j + \dfrac{1}{18}u_{j+1}\right), & j \equiv 2\,(\mathrm{mod}3) \\ \dfrac{1}{h}\left(u_{j-3} - \dfrac{7}{2}u_{j-2} + 5u_{j-1} - \dfrac{5}{2}u_j\right), & j \equiv 0\,(\mathrm{mod}3) \end{cases} \tag{3.9}$$

- DG-P^3 (5-point scheme):

$$\frac{d}{dt}u_j = \begin{cases} \dfrac{1}{h}\left(-\dfrac{19}{64}u_{j-1} + \dfrac{145}{18}u_j - \dfrac{153}{32}u_{j+1} + \dfrac{43}{16}u_{j+2} - \dfrac{121}{192}u_{j+3}\right), & j \equiv 1\,(\mathrm{mod}4) \\ \dfrac{1}{h}\left(-\dfrac{3}{8}u_{j-2} + \dfrac{11}{6}u_{j-1} - \dfrac{7}{4}u_j + \dfrac{1}{2}u_{j+1} - \dfrac{5}{24}u_{j+2}\right), & j \equiv 2\,(\mathrm{mod}4) \\ \dfrac{1}{h}\left(\dfrac{31}{64}u_{j-3} - \dfrac{101}{48}u_{j-2} + \dfrac{125}{32}u_{j-1} - \dfrac{39}{16}u_j + \dfrac{29}{192}u_{j+1}\right), & j \equiv 3\,(\mathrm{mod}4) \\ \dfrac{1}{h}\left(-u_{j-4} + \dfrac{13}{3}u_{j-3} - \dfrac{15}{2}u_{j-2} + 7u_{j-1} - \dfrac{17}{6}u_j\right), & j \equiv 0\,(\mathrm{mod}4) \end{cases} \tag{3.10}$$

- DG-P^4 (6-point scheme):

$$\frac{d}{dt}u_j = \begin{cases} \frac{1}{h}\Big(-\frac{399}{625}u_{j-1} + \frac{7913}{1500}u_j - \frac{1298}{125}u_{j+1} + \frac{1173}{125}u_{j+2} - \frac{1697}{375}u_{j+3} \\ \qquad + \frac{2221}{2500}u_{j+4}\Big), \qquad j \equiv 1\,(\mathrm{mod}5) \\ \frac{1}{h}\Big(-\frac{59}{625}u_{j-2} + \frac{361}{500}u_{j-1} - \frac{83}{750}u_j - \frac{139}{250}u_{j+1} + \frac{7}{250}u_{j+2} \\ \qquad + \frac{83}{7500}u_{j+3}\Big), \qquad j \equiv 2\,(\mathrm{mod}5) \\ \frac{1}{h}\Big(\frac{281}{625}u_{j-3} - \frac{3497}{1500}u_{j-2} + \frac{1936}{375}u_{j-1} - \frac{562}{125}u_j + \frac{593}{375}u_{j+1} \\ \qquad - \frac{2747}{7500}u_{j+2}\Big), \qquad j \equiv 3\,(\mathrm{mod}5) \\ \frac{1}{h}\Big(-\frac{219}{625}u_{j-4} + \frac{2753}{1500}u_{j-3} - \frac{1001}{250}u_{j-2} + \frac{1251}{250}u_{j-1} - \frac{1939}{750}u_j \\ \qquad + \frac{251}{2500}u_{j+1}\Big), \qquad j \equiv 4\,(\mathrm{mod}5) \\ \frac{1}{h}\Big(u_{j-5} - \frac{21}{4}u_{j-4} + \frac{34}{3}u_{j-3} - 13u_{j-2} + 9u_{j-1} \\ \qquad - \frac{37}{12}u_j\Big), \qquad j \equiv 0\,(\mathrm{mod}5) \end{cases} \tag{3.11}$$

- DG-P^5 (7-point scheme):

$$\frac{d}{dt}u_j = \begin{cases} \frac{1}{h}\Big(-\frac{1121}{1296}u_{j-1} + \frac{8071}{1080}u_j - \frac{7765}{432}u_{j+1} + \frac{7725}{324}u_{j+2} - \frac{7045}{432}u_{j+3} + \frac{1391}{216}u_{j+4} \\ \qquad - \frac{6901}{6480}u_{j+5}\Big), \qquad j \equiv 1\,(\mathrm{mod}6) \\ \frac{1}{h}\Big(\frac{17}{81}u_{j-2} - \frac{143}{135}u_{j-1} + \frac{457}{108}u_j - \frac{502}{81}u_{j+1} + \frac{112}{27}u_{j+2} - \frac{43}{27}u_{j+3} \\ \qquad + \frac{421}{1620}u_{j+4}\Big), \qquad j \equiv 2\,(\mathrm{mod}6) \\ \frac{1}{h}\Big(\frac{5}{16}u_{j-3} - \frac{77}{40}u_{j-2} + \frac{83}{16}u_{j-1} - \frac{71}{12}u_j + \frac{59}{16}u_{j+1} - \frac{13}{8}u_{j+2} \\ \qquad + \frac{67}{240}u_{j+3}\Big), \qquad j \equiv 3\,(\mathrm{mod}6) \\ \frac{1}{h}\Big(-\frac{32}{81}u_{j-4} + \frac{649}{270}u_{j-3} - \frac{667}{108}u_{j-2} + \frac{721}{81}u_{j-1} - \frac{169}{27}u_j + \frac{101}{54}u_{j+1} \\ \qquad - \frac{559}{1620}u_{j+2}\Big), \qquad j \equiv 4\,(\mathrm{mod}6) \\ \frac{1}{h}\Big(\frac{251}{1296}u_{j-5} - \frac{1309}{1080}u_{j-4} + \frac{1399}{432}u_{j-3} - \frac{1579}{324}u_{j-2} + \frac{2119}{432}u_{j-1} - \frac{485}{216}u_j \\ \qquad - \frac{41}{6480}u_{j+1}\Big), \qquad j \equiv 5\,(\mathrm{mod}6) \\ \frac{1}{h}\Big(-u_{j-6} + \frac{31}{5}u_{j-5} - \frac{65}{4}u_{j-4} + \frac{70}{3}u_{j-3} - 20u_{j-2} + 11u_{j-1} \\ \qquad - \frac{197}{60}u_j\Big), \qquad j \equiv 0\,(\mathrm{mod}6) \end{cases} \tag{3.12}$$

We can also analyze the dispersion relations of these finite difference schemes and get the same results as those in section 2.

To ensure that different schemes use the same degrees of freedom in one wavelength, we let $h_{DG-P^q} = (q+1)h$, $h_{FD} = h$, then we introduce

$$\tilde{k} = kh, \qquad \tilde{\omega}^* = \bar{\omega}h, \qquad \tilde{\omega} = \omega h$$

to compare different schemes which have different cell lengths h and different polynomial degrees q. We found that for DG-P^q, $q = 1$ to 5, $\boldsymbol{A}$ has $q+1$ different eigenvalues, which is consistent with our previous assumption. Figure 3.1 shows the real parts of dispersion relations for the DG schemes and some central FD schemes. Figures 3.2 and 3.3 give the dissipation coefficients diagram and relative dispersion error diagram respectively. It can be seen that the DG schemes have better dispersive properties than the FD schemes and the increasing of the order of the DG schemes can reduce the dispersion error.

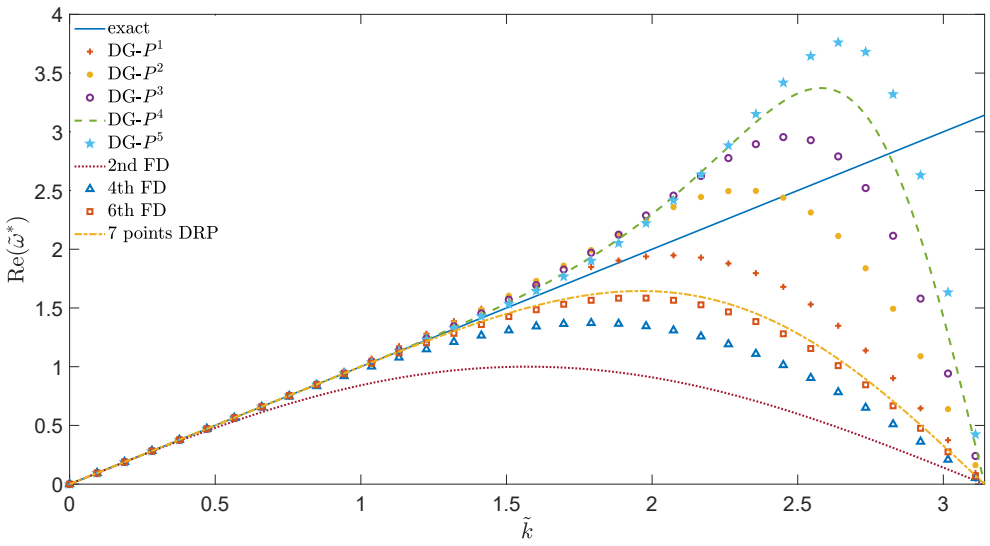

Fig. 3.1. Dispersion relations for DG schemes and central FD schemes.

3.1 Long wave components

In order to better compare the dispersion properties of different schemes in long waves (waves for which $\tilde{k}$ is relatively small), we define the well resolved range of wave numbers

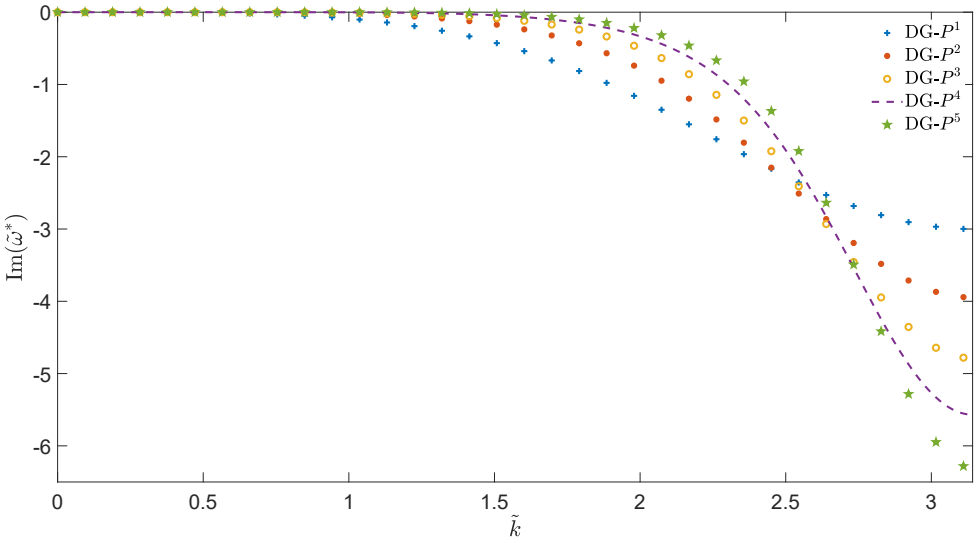

Fig. 3.2. Dissipation coefficients for DG schemes.

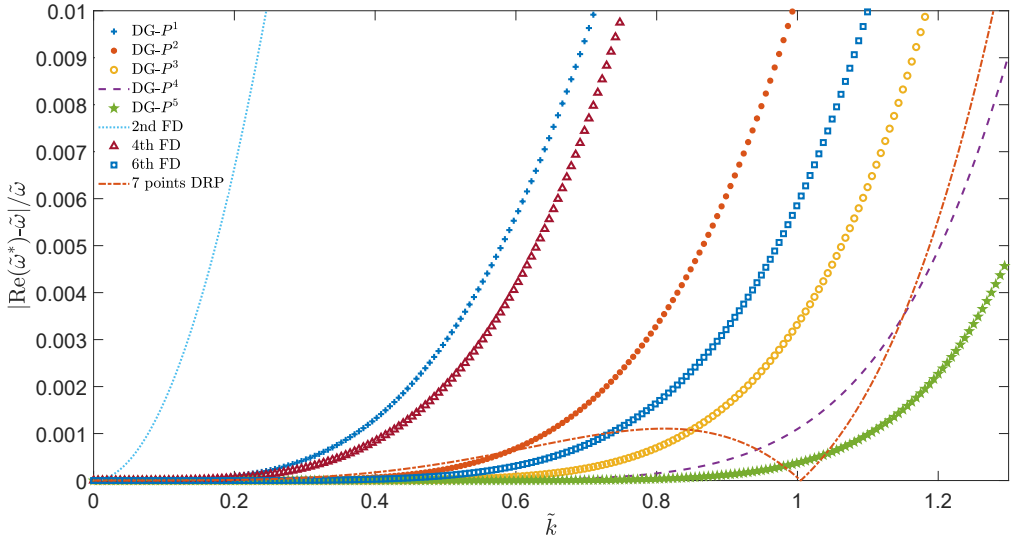

Fig. 3.3. Relative errors of $\mathrm{Re}(\tilde{\omega})$ for DG schemes and central FD schemes.

by requiring

$$|\mathrm{Re}(\tilde{\omega}) - \tilde{k}| < 0.01$$

Then we can find the maximum resolved wave number and the corresponding minimum number of unknowns per wavelength. Table 3.1 lists the maximum resolved wave numbers and minimum numbers of unknowns per wavelength for DG schemes and central FD schemes, respectively. This indicates that the DG schemes can resolve more small scale features than the same order FD schemes can and high order DG schemes can better resolve these small scale features.

scheme	wave number	unknowns per wavelength
DG-P^1	0.7716	8.1430
DG-P^2	0.9942	6.3193
DG-P^3	1.1567	5.4318
DG-P^4	1.2754	4.9266
DG-P^5	1.3653	4.6020
FD 2nd order	0.3925	16.0075
FD 4th order	0.7980	7.8733
FD 6th order	1.0841	5.7955
optimized 7-point DRP	1.2469	5.0390

Table 3.1. Maximum resolved wave number and minimum number of unknowns per wavelength for DG schemes, central FD schemes and the DRP scheme.

3.2 Short wave components

For short wave components, their $\tilde{k}$'s are larger, and all schemes have large dispersion errors. Therefore, in order to ensure the reliability of the computation results, the short wave components must be automatically removed from the computation as soon as they are generated. This is not possible for the original DRP scheme and other central FD schemes, as they are strictly non-dissipative. For this reason, an artificial selective damping (ASD) term was added to the DRP scheme [37]. In fact, it provides a dissipation term with dissipation coefficient inversely related to wavelength.

As for a DG scheme, for example, DG-P^1, we can see from Figure 2.1 that the dissipative term exists for the scheme. Therefore, the short wave components of the

solution can be automatically removed without any modification. Examples 6.4 and 6.5 in section 6 illustrate this point.

4 Group velocity consideration and numerical stability

In section 3, we have given the relation between $\mathrm{Re}(\tilde{\omega})$ and $\tilde{k}$ of several DG and FD schemes. The phase velocity is defined by:

$$c_p = \frac{\mathrm{Re}(\tilde{\omega})}{\tilde{k}} \tag{4.1}$$

and it represents the propagation speed of each single wave. However, in order to study the effect of numerical schemes on high frequency waveforms more accurately, we need to introduce the concept of group velocity.

Considering that u_h is related to k, we use $u_h(k,x,t)$ instead of $u_h(x,t)$. In order to establish the group velocity formula of DG solutions, we first propose the lemmas:

Lemma 4.1. If each eigenvalue of $\boldsymbol{A}$ is a single eigenvalue, $u_h(k,x,t)$ is continuous with respect to k in $(-\infty,\infty)$.

Proof. From (2.7), we know that we only need to prove that $\bar{\omega}_n(k)$, $\gamma_n(k)$ and $\beta_{mn}(k)$ are continuous with respect to k. Noticing that every elements of $\boldsymbol{A}$ and α are continuous with respect to k, from the matrix perturbation theory in [38], we know that eigenvalues, the left and right eigenvectors of $\boldsymbol{A}$'s single eigenvalue are continuous with respect to the elements of $\boldsymbol{A}$. Therefore, the desired results can be obtained.

Lemma 4.2. Take k_0 as an arbitrary positive number, when $|k| > k_0$, the following inequalities hold:

$$|u_h(k,x,t)| < 2(q+1)\sqrt{\frac{(2q+1)(q+1)(k_0h+\pi)}{k_0h}} \tag{4.2a}$$

$$\left|\frac{\partial u_h}{\partial t}(k,x,t)\right| < \frac{2(2q+1)(q+1)^2}{h}\sqrt{\frac{(q+1)(k_0h+\pi)}{k_0h}}(2\sqrt{2q+1}+\sqrt{2}M_0) \tag{4.2b}$$

for all $x \in (-\infty,\infty)$ and $t > 0$. Here, $M_0 = \max\limits_{s=0,1,\cdots,q} ||\varphi_s^{'}(\xi)||_{L^2(-1,1)}$.

Proof. The proof of this lemma is provided in the appendix; see section A.

Based on Lemma 4.1 and Lemma 4.2, we can get the following theorem to describe the relationship between DG solutions of single and composite waves.

Theorem 4.1. Change the initial value of equation (2.1) to:

$$u(x,0) = f(x) \tag{4.3}$$

Suppose that:

- Each eigenvalue of $\boldsymbol{A}$ is a single eigenvalue.
- $f(x) \in L^1(-\infty,\infty)$. That is to say, Fourier transform can be done for it:

$$\hat{f}(k) = \frac{1}{2\pi}\int_{-\infty}^{\infty} f(x)e^{-ikx}dx, \quad f(x) = \int_{-\infty}^{\infty}\hat{f}(k)e^{ikx}dk \tag{4.4}$$

- $\hat{f}(k) \in L^1(-\infty,\infty) \cap C(-\infty,\infty)$.

Here, L^1 and C are symbols of absolute integrable functions and continuous functions, respectively. Then

- The improper integral:

$$\int_{-\infty}^{\infty}\hat{f}(k)u_h(k,x,t)dk \tag{4.5}$$

  converges.

- The corresponding DG solution of equation (2.1) is:

$$\tilde{u}_h(x,t) = \int_{-\infty}^{\infty}\hat{f}(k)u_h(k,x,t)dk \tag{4.6}$$

Proof. The proof of this theorem is provided in the appendix; see section B.

Next, we consider the group velocity of DG solutions on a line $x = ct+\xi$, we can get:

$$\begin{aligned}\tilde{u}_h(x,t) &= \int_{-\infty}^{\infty}\hat{f}(k)u_h(k,x,t)dk \\ &= \int_{-\infty}^{\infty}\hat{f}(k)\left(r(\eta)e^{i\theta(\eta)}e^{ik\xi}e^{it(kc-\bar{\omega}_{0r})}e^{\bar{\omega}_{0i}t} + \sum_{n=1}^{p}\gamma_n u_h^n(x,0)e^{-i\bar{\omega}_{nr}t}e^{\bar{\omega}_{ni}t}\right)dk\end{aligned} \tag{4.7}$$

It is easy to verify that the effect of virtual waves can be dissipated to negligible levels when $t \to \infty$. Let $\Phi(k) = kc - \bar{\omega}_{0r}$. The method of stationary phase [21] implies that the most significant contribution to the integral (4.7) occurs when:

$$\Phi^{'}(k) = c - \frac{d\bar{\omega}_{0r}}{dk} = 0 \tag{4.8}$$

Thus, the principal contribution of the components at wave number k is felt when moving at the group velocity

$$c_g = \frac{d\bar{\omega}_{0r}}{dk} = \frac{d\mathrm{Re}(\tilde{\omega})}{d\tilde{k}} \tag{4.9}$$

Figure 4.4 shows the variation of group velocity with $\tilde{k}$ in different schemes. Figure 4.5 shows a locally enlarged image. We can see that, unlike FD schemes, the group velocities of DG schemes are larger than the exact group velocity in a considerable range. Therefore, DG scheme usually produces "leading waves" (which are removed by numerical dissipation), rather than "trailing waves" in FD schemes. Moreover, compared with FD schemes of the same order, the "resolvable ranges" of group velocities of DG schemes are larger.

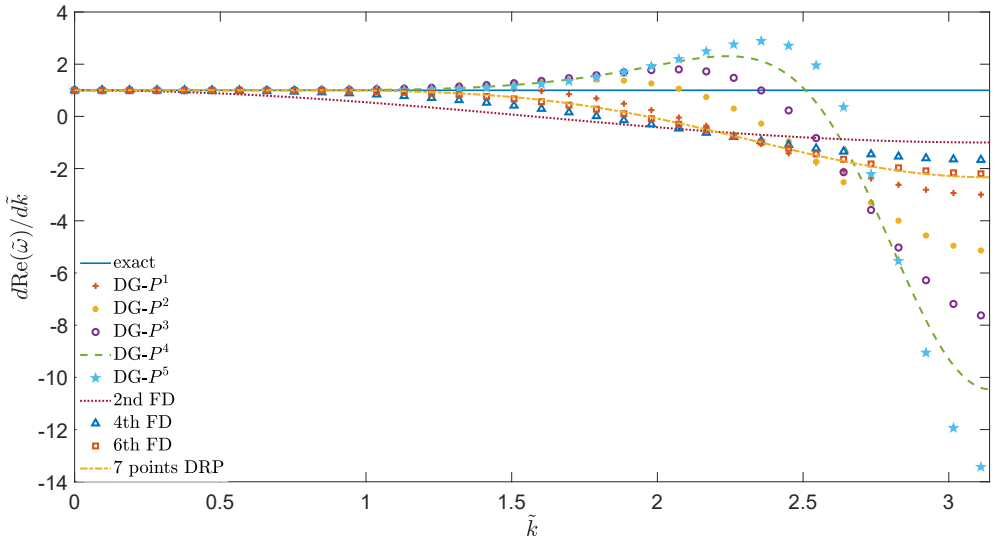

Fig. 4.4. Group velocity comparison for DG schemes and central FD schemes.

The finite difference schemes on non-symmetric stencils often produce numerical instability, especially when they violate the upwind property. However, central difference

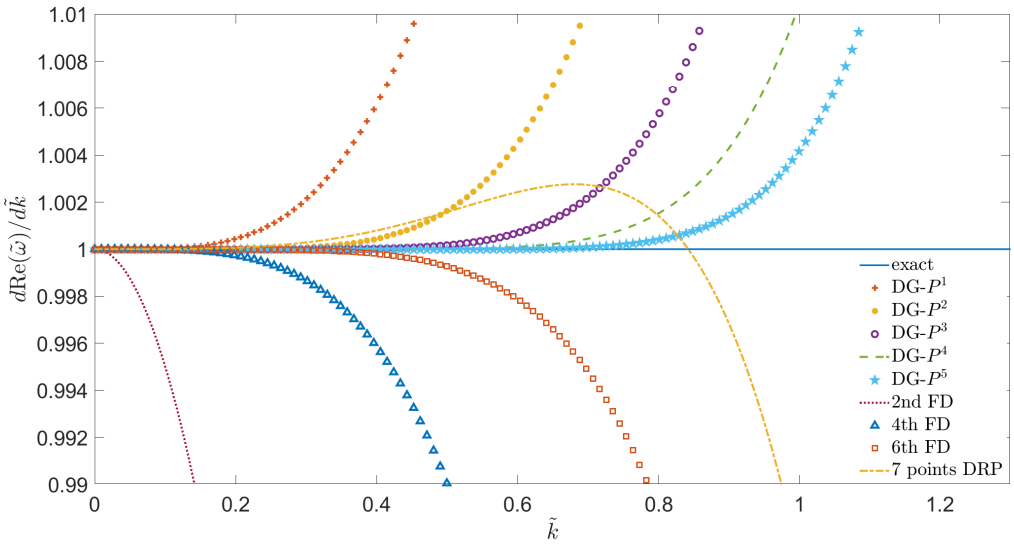

Fig. 4.5. An enlarged image for Figure 4.4.

schemes, including DRP scheme, do not cause this problem. On the other hand, for DG schemes with an appropriate numerical flux, the L^2 stability [28] for scalar conservation laws ensures that the L^2 norm of DG solution does not increase with time. For solutions with strong discontinuities, various limiters (TVD, TVB, WENO et al) [9, 41] are designed to obtain nonlinear stability and to control spurious oscillations.

5 DG schemes with upwind-biased flux

It should be noted that the DG schemes do not necessarily use upwind numerical fluxes. For example, in [25], Meng and Shu proposed an upwind-biased numerical flux:

$$\hat{u}_{j+1/2} = \theta u^-_{j+1/2} + (1-\theta)u^+_{j+1/2} \tag{5.1}$$

where $\theta = 1$ corresponds to the numerical flux in the common upwind form. The stability of the scheme and the optimal error estimate are proved in the case of $\theta > 1/2$. Our analytical method for dispersion properties of DG schemes can be easily applied to this kind of upwind-biased flux DG. At this time, (2.5) becomes:

$$\bar{\omega}\beta_l = \frac{i(2l+1)}{h}\sum_{m=0}^{q}\left(\int_{-1}^{1}\varphi_m\varphi_l' d\xi + (\theta + (1-\theta)e^{ikh}(-1)^m)(-1+e^{-ikh}(-1)^l)\right)\beta_m \tag{5.2}$$

The maximum resolved wave number and minimum number of unknowns per wavelength results for $\theta = 0.75$ and $\theta = 2$ are given in Table 5.2 and Table 5.3 respectively. From the results, we can see that the dispersion properties of upwind-biased DG schemes depend on both θ and the polynomial degree q.

scheme	wave number	unknowns per wavelength
DG-P^1 $\theta = 0.75$	0.5770	10.8885
DG-P^2 $\theta = 0.75$	0.9333	6.7320
DG-P^3 $\theta = 0.75$	1.3338	4.7108
DG-P^4 $\theta = 0.75$	1.5967	3.9350
DG-P^5 $\theta = 0.75$	1.3282	4.7305

Table 5.2. Maximum resolved wave number and minimum number of unknowns per wavelength for DG scheme with $\theta = 0.75$.

scheme	wave number	unknowns per wavelength
DG-P^1 $\theta = 2$	0.6613	9.5011
DG-P^2 $\theta = 2$	1.3548	4.6376
DG-P^3 $\theta = 2$	1.0297	6.1022
DG-P^4 $\theta = 2$	1.1665	5.3863
DG-P^5 $\theta = 2$	1.4264	4.4050

Table 5.3. Maximum resolved wave number and minimum number of unknowns per wavelength for DG scheme with $\theta = 2$.

6 Numerical results

Now we validate our conclusion with a series of numerical results. The numerical examples we choose mainly come from the ICASE workshop [17] and a series of related studies, which have shown that these examples can evaluate the performance of numerical schemes in CAA well.

Example 6.1. In this example, we consider the linear convection equation:

$$u_t + u_x = 0 \tag{6.1a}$$

$$u(x,0) = \frac{1}{2} e^{-(\ln 2)\left(\frac{x}{b}\right)^2} \tag{6.1b}$$

We can easily get the analytic solution of this equation is:

$$u(x,t) = \frac{1}{2} e^{-(\ln 2)\left(\frac{x-t}{b}\right)^2} \tag{6.2}$$

by means of the characteristic line method. We select a sufficiently large computational region ($[-800, 1000]$) so that the compactly supported boundary conditions can be applied to both boundaries. In order to ensure the consistency of the degrees of freedom of each scheme in one wavelength, we let $h_{FD} = 1$, $h_{DG-P^q} = q + 1$, $\Delta t = 1/30h$. In all finite difference schemes, no filters are used. The settings of boundary conditions and filter-free computation are also applied to Examples 6.2 to 6.5. After the spatial discretization by DG or FD schemes, we use the optimal third order TVD Runge-Kutta method [29] to advance the solution to $t = 400$. The results of the FD schemes and DG schemes are shown in Figure 6.1. As we can see, all the FD solutions, including the DRP solution, are trailed by noticeable spurious dispersive waves. However, this phenomenon is almost not noticeable for the DG solutions. The DG schemes have very nice dispersive properties. On the other hand, the location and amplitude of the solution bump are resolved by the optimized 7-point DRP scheme and by DG-P^5 (which is also a 7-point scheme) almost equally well.

Figure 6.2 shows the results of upwind-biased DG schemes with different θ's. In order to make the results more differentiated, we changed b to 1.5. Notice that the upwind DG scheme is the case when $\theta = 1$. As we can see from the figure, the results are irregular: for DG-P^1, $\theta = 1$ performs best; for DG-P^2 and DG-P^5, $\theta = 2$ performs best; for DG-P^3, $\theta = 0.75$ performs best; for DG-P^4, the three schemes perform similarly.

Example 6.2. In this example, we consider the linearized Euler equations in the absence of a mean flow:

$$u_t + p_x = 0 \tag{6.3a}$$

$$p_t + u_x = 0 \tag{6.3b}$$

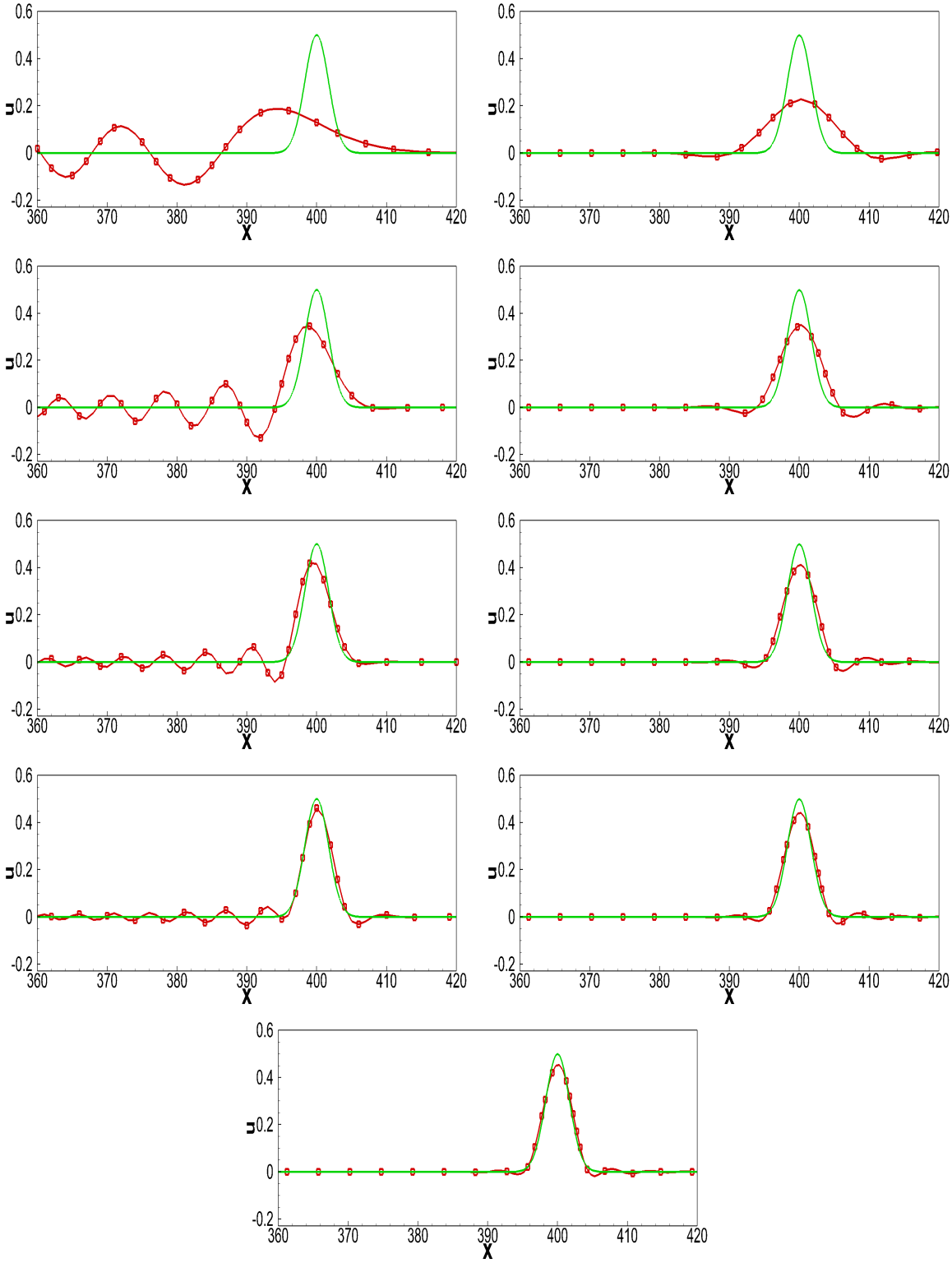

Fig. 6.1. Comparisons between the numerical and exact solutions of the convective wave equation. $b = 2$, $t = 400$, $h_{FD} = 1$, $h_{DG-P^q} = q + 1$. Lines without square symbols correspond to exact solutions while lines with square symbols correspond to numerical solutions. The subgraphs from top to bottom on the left correspond to FD schemes of order 2, 4, 6, optimized 7-point DRP scheme, and the subgraphs from top to bottom on the right correspond to DG $P^1 - P^4$. The bottom subgraph corresponds to DG-P^5.

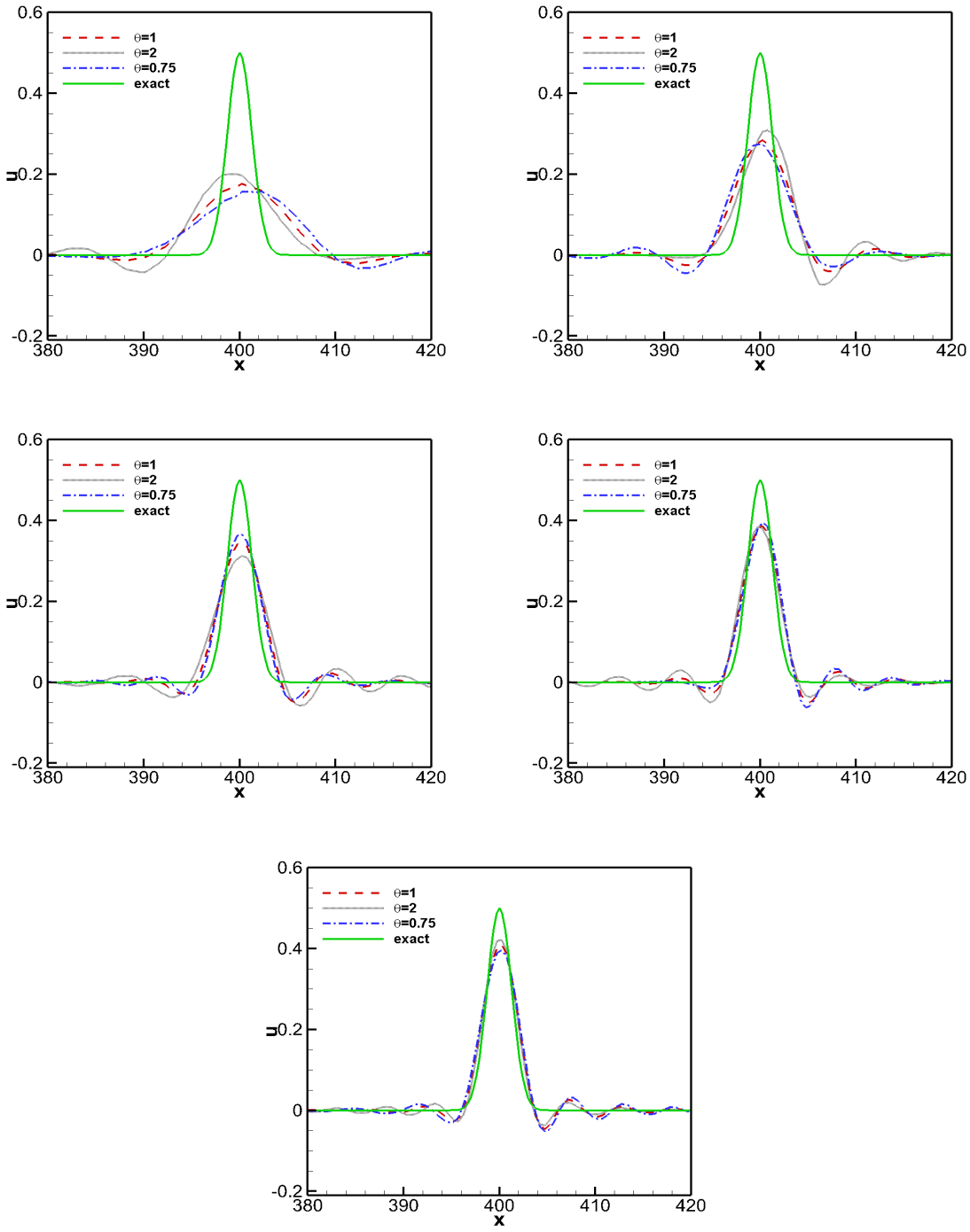

Fig. 6.2. Comparisons between the numerical and exact solutions of the convective wave equation. $b = 1.5$, $t = 400$, $h_{DG-P^q} = q + 1$. Subgraphs correspond to DG-$P^1 - P^5$ in the order of left to right and top to bottom, respectively.

with initial conditions:

$$u(x,0) = e^{-(\ln 2)\left(\frac{x}{b}\right)^2} \tag{6.4a}$$

$$p(x,0) = 0 \tag{6.4b}$$

The exact solutions are given by:

$$u(x,t) = \frac{1}{2}[u(x-t,0) + u(x+t,0)] \tag{6.5a}$$

$$p(x,t) = \frac{1}{2}[u(x-t,0) - u(x+t,0)] \tag{6.5b}$$

The third-order RK scheme is used for time discretizations. The computational region is $[-420, 420]$, $\Delta t = 1/30h$. Figures 6.3 and 6.4 show the results of the FD schemes and the DG schemes, respectively. Just like the previous example, we can see that the DG schemes yield good results without spurious trailing waves. Also, the location and amplitude of the solution bump are resolved by the optimized 7-point DRP scheme and by DG-P^5 almost equally well.

Example 6.3. Now we consider the dimensionless linearized Euler equations with a uniform mean flow:

$$\rho_t + M\rho_x + u_x = 0 \tag{6.6a}$$

$$u_t + Mu_x + p_x = 0 \tag{6.6b}$$

$$p_t + Mp_x + u_x = 0 \tag{6.6c}$$

where M is the flow Mach number. Let the initial conditions be

$$u(x,0) = 0 \tag{6.7a}$$

$$p(x,0) = e^{-(\ln 2)\left(\frac{x-200}{b}\right)^2} + e^{-(\ln 2)\left(\frac{x+200}{b}\right)^2} \tag{6.7b}$$

$$\rho(x,0) = p(x,0) + e^{-(\ln 2)\left(\frac{x}{b}\right)^2}. \tag{6.7c}$$

Using the method of characteristics, we can get the exact solution as follows:

$$u(x,t) = \frac{1}{2}[p(x-(M+1)t,0) - p(x-(M-1)t,0)] \tag{6.8a}$$

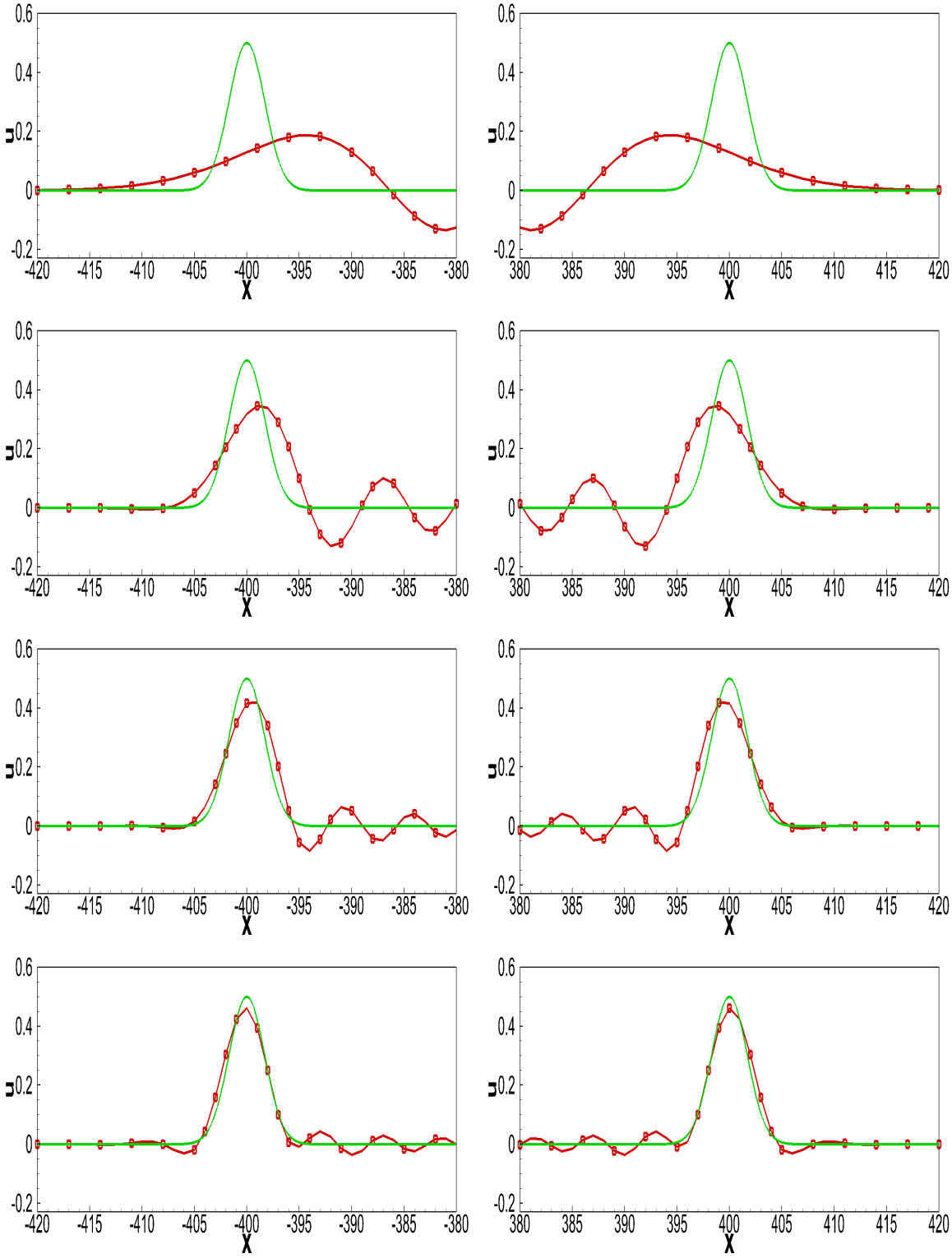

Fig. 6.3. Comparisons between the numerical and exact solutions of the linearized Euler equations in the absence of a mean flow. $b = 2$, $t = 400$, $h = 1$. Lines without square symbols correspond to the exact solutions while lines with square symbols correspond to the numerical solutions. The subgraphs from top to bottom correspond to FD schemes of orders 2, 4, 6, and the optimized 7-point DRP scheme. The graphs on the left correspond to the upstream and the graphs on the right correspond to the downstream.

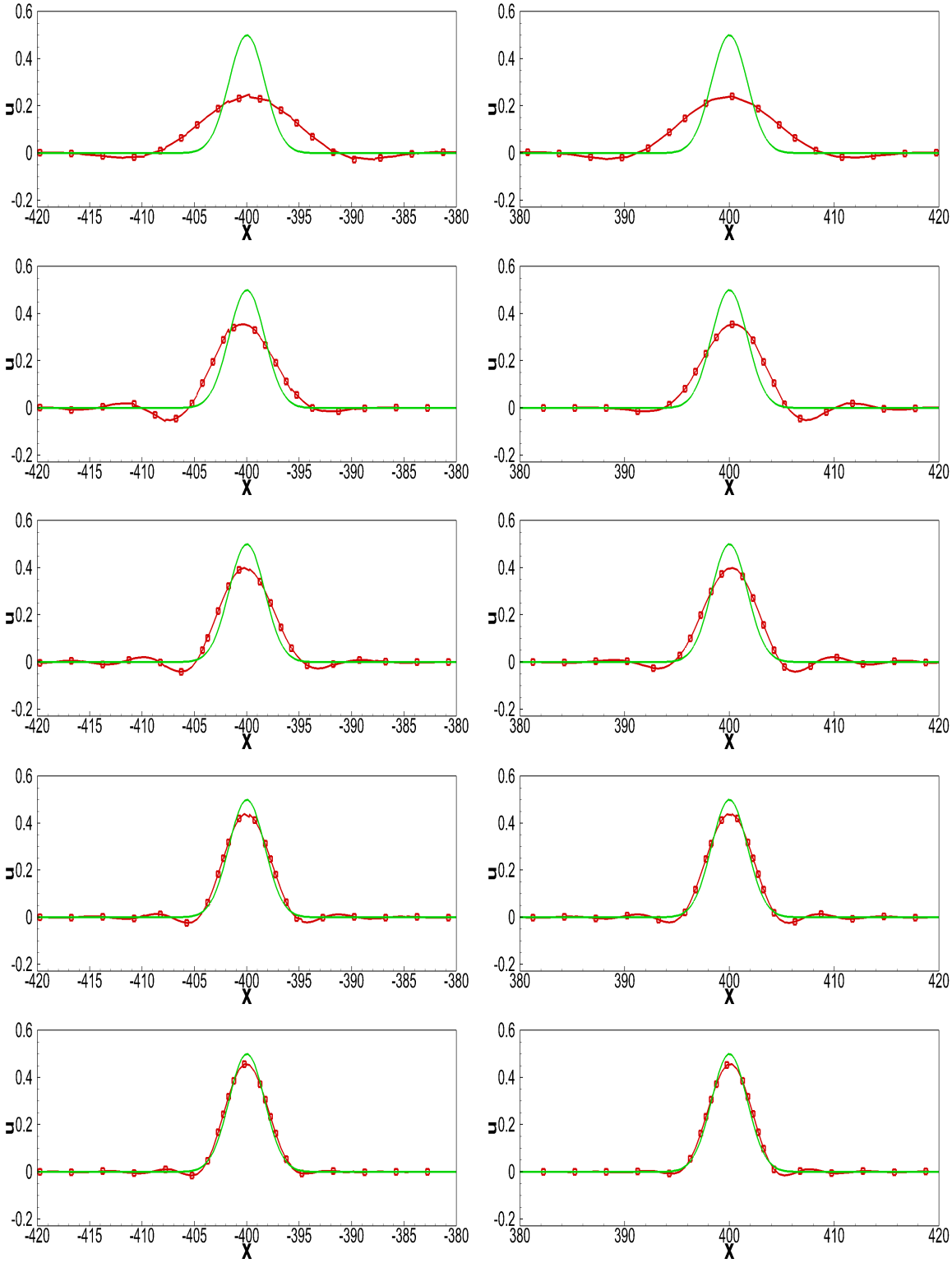

Fig. 6.4. Comparisons between the numerical and exact solutions of the linearized Euler equations in the absence of a mean flow. $b = 2$, $t = 400$, $h_{DG-P^q} = q + 1$. Lines without square symbols correspond to the exact solutions while lines with square symbols correspond to the numerical solutions. The subgraphs from top to bottom correspond to DG-P^1 to P^5. The graphs on the left correspond to the upstream and the graphs on the right correspond to the downstream.

$$p(x,t) = \frac{1}{2}[p(x-(M+1)t,0) + p(x-(M-1)t,0)] \tag{6.8b}$$

$$\rho(x,t) = \frac{1}{2}[p(x-(M+1)t,0) + p(x-(M-1)t,0)] - p(x-Mt,0) + \rho(x-Mt,0) \tag{6.8c}$$

As before, we use the third-order RK method as the time discretization method. The computational region is $[-1000, 2300]$. $\Delta t = 1/(30(M+1))h$. Figures 6.5 and 6.6 show the results of the FD schemes and the DG schemes, respectively. We can see that, similar to the previous examples, the DG schemes have achieved good results. In particular, the resolutions of the spikes by the optimized 7-point DRP scheme and by DG-P^5 are comparable.

Example 6.4. In this example, we test the ability of DG scheme to resolve short wave component solutions by an initial value problem of piecewise constants for linearized Euler equations (6.9), following the earlier work of Tam [31, 37].

$$u_t + p_x = 0 \tag{6.9a}$$

$$p_t + u_x = 0 \tag{6.9b}$$

$$u(x,0) = 0 \tag{6.9c}$$

$$p(x,0) = H(x+M) - H(x-M) \tag{6.9d}$$

where $H(x)$ is the unit step function. The wave number spectrum of this initial condition extends to a large extent beyond $[0, \pi]$. The exact solutions of (6.9) are given by:

$$u(x,t) = \frac{1}{2}[H(x-t+M) - H(x-t-M)] - \frac{1}{2}[H(x+t+M) - H(x+t-M)] \tag{6.10a}$$

$$p(x,t) = \frac{1}{2}[H(x-t+M) - H(x-t-M)] + \frac{1}{2}[H(x+t+M) - H(x+t-M)] \tag{6.10b}$$

We choose the computational region as $[-420, 800]$. $\Delta t = 1/30h$. The numerical results of the DG-P^1 scheme, the DRP scheme and the DRP-ASD scheme are shown in Figure 6.7. From the figure, we can see that the solution of the original DRP scheme is polluted by the short wave components when dealing with the initial value problem with a

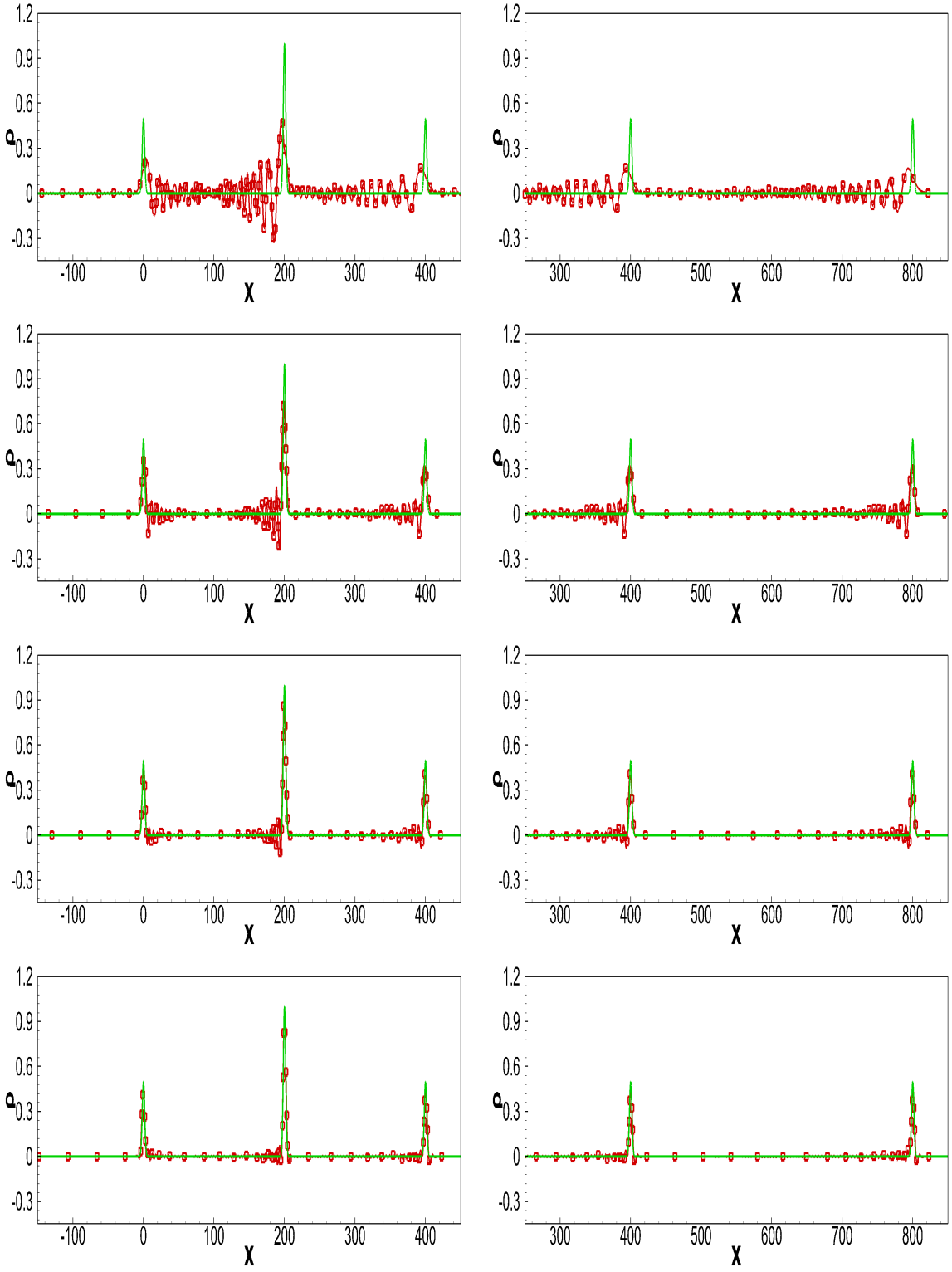

Fig. 6.5. Comparisons between the numerical and exact solutions of the dimensionless linearized Euler equations with a uniform mean flow. $b = 2$, $t = 400$, $h = 1$. Lines without square symbols correspond to the exact solutions while lines with square symbols correspond to the numerical solutions. The subgraphs from top to bottom correspond to FD schemes of orders 2, 4, 6, and the optimized 7-point DRP scheme. The graphs on the left correspond to the upstream and the graphs on the right correspond to the downstream.

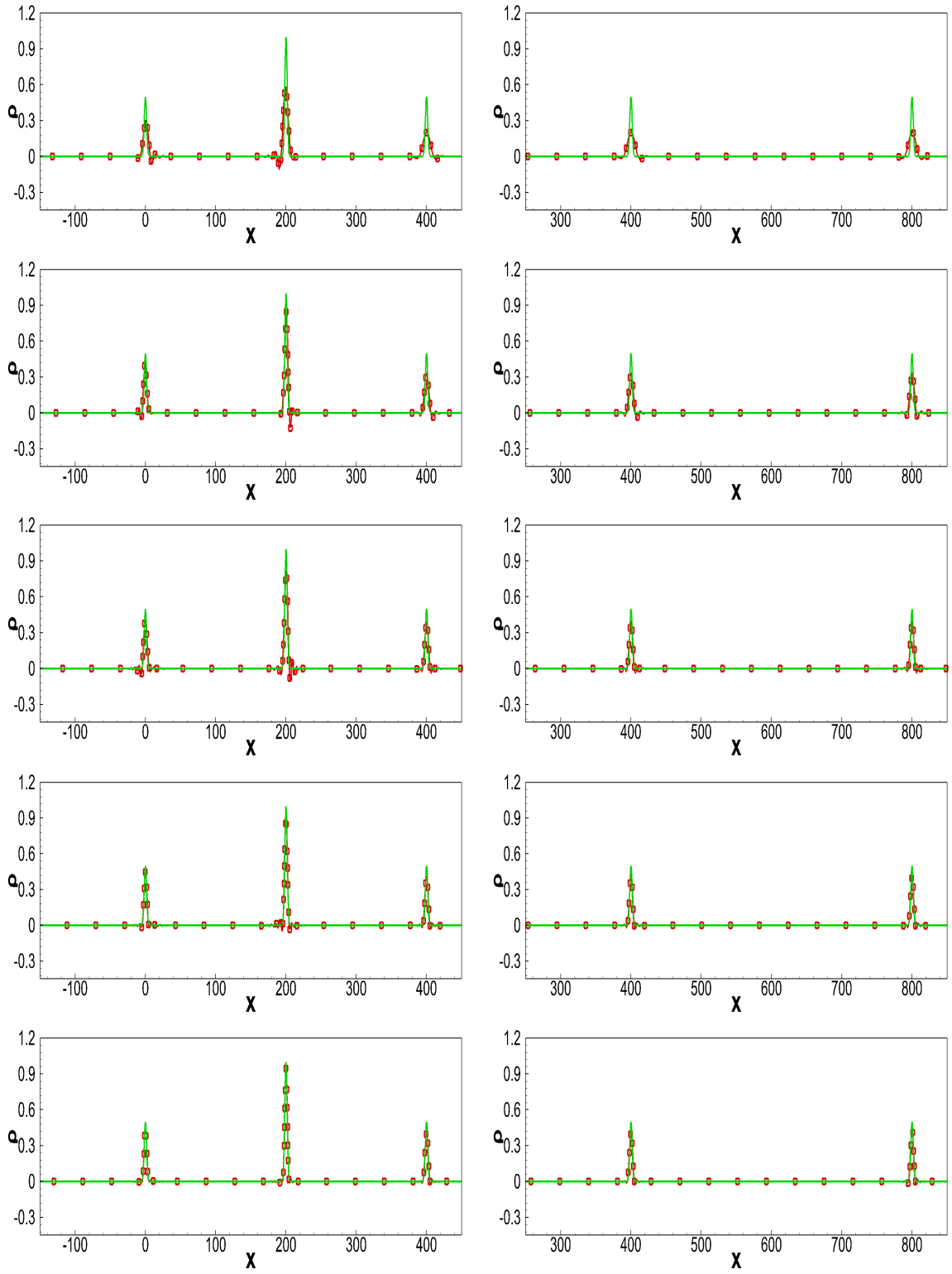

Fig. 6.6. Comparisons between the numerical and exact solutions of the dimensionless linearized Euler equations with a uniform mean $b = 2$, $t = 400$, $h_{DG-P^q} = q + 1$. Lines without square symbols correspond to the exact solutions while lines with square symbols correspond to the numerical solutions. The subgraphs from top to bottom correspond to DG-P^1 to P^5. The graphs on the left correspond to the upstream and the graphs on the right correspond to the downstream.

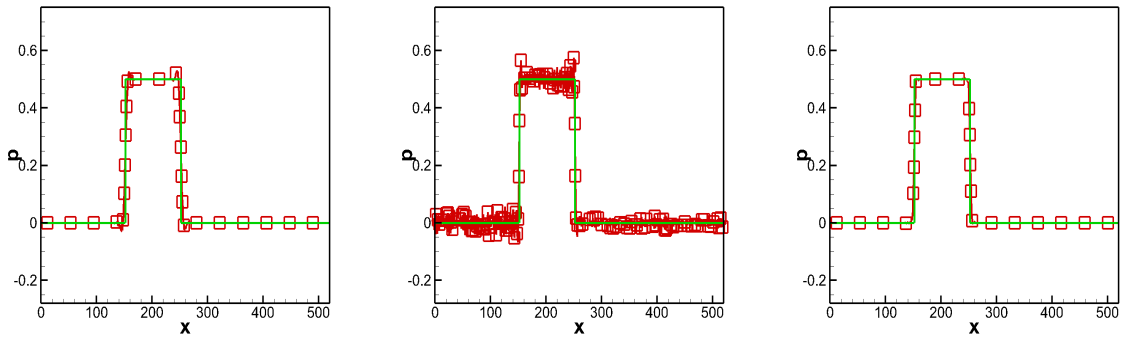

Fig. 6.7. Comparisons between the numerical and exact solutions of (6.9). $h_{DG-P^1} = 2$, $h_{DRP} = h_{DRP-ASD} = 1$, $t_{end} = 202$, $M = 50$. Lines without square symbols correspond to the exact solutions while lines with square symbols correspond to the numerical solutions. The subgraphs from left to right correspond to DG-P^1, DRP, DRP-ASD.

relatively large proportion of short wave components. After adding an artificial selective damping (ASD) term, the solution has been greatly improved. On the other hand, the DG scheme can resolve the short wave component solution without any modification.

Example 6.5. We continue to test the resolution ability of the DG scheme for short wave component solutions through a nonlinear scalar problem [31, 37]:

$$u_t + u_x + \frac{\gamma+1}{4}(u^2)_x = 0 \tag{6.11a}$$

$$u(x,0) = h_0 e^{-(\ln 2)\left(\frac{x}{b}\right)^2} \tag{6.11b}$$

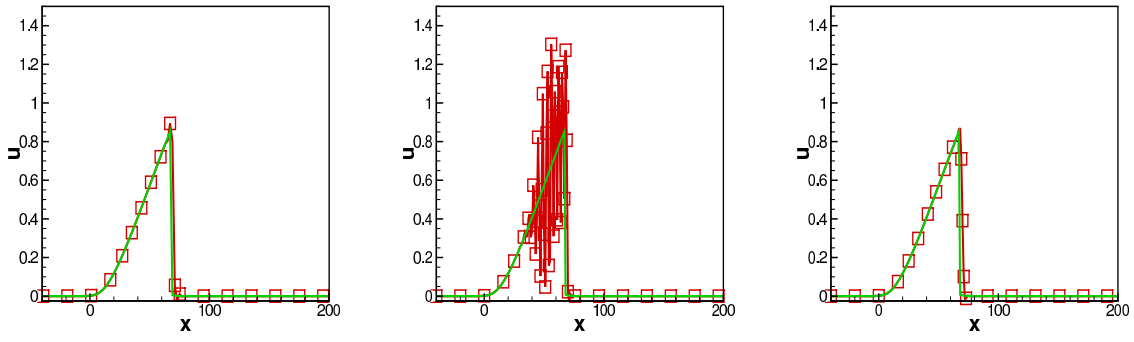

Fig. 6.8. Comparisons between the numerical and exact solutions of (6.11). $h_{DG-P^1} = 2$, $h_{DRP} = h_{DRP-ASD} = 1$, $t_{end} = 36$, $h_0 = 1$, $b = 12$, $\gamma = 1.4$. Lines without square symbols correspond to the exact solutions while lines with square symbols correspond to the numerical solutions. The subgraphs from left to right correspond to DG-P^1, DRP, and DRP-ASD.

The computational area is selected as $[-400, 400]$, and the time step is taken as:

$$\Delta t = \frac{1}{30(1 + (\gamma + 1)/2 \max_j |\bar{u}_j|)} h. \tag{6.12}$$

Figure 6.8 shows the results of the three schemes for $t_{end} = 36$. Similar to the previous example, the original DRP scheme cannot resolve the short wave component solution well. It needs an artificial selective damping modification. The DG scheme, on the other hand, can resolve them very well.

Example 6.6. The nozzle flow is a classical test problem which has been studied by many researchers because of its complex CAA characteristics and important application value [13, 30, 32, 34]. We consider sound generation in a one-dimension supersonic nozzle flow induced by the passage of an entropy pulse. Dimensionless variables with the following scales are used.

- Length scale: D, the diameter of the uniform duct upstream of the nozzle.
- Velocity scale: a_0, speed of the sound in the uniform duct upstream of the nozzle.
- Time scale: D/a_0.
- Density scale: ρ_0, density of gas in the uniform duct upstream of the nozzle.
- Pressure scale: $\rho_0 a_0^2$

The governing equations are:

$$\rho_t + (\rho u)_x + \frac{A_x}{A}\rho u = 0 \tag{6.13a}$$

$$(\rho u)_t + (\rho u^2 + p)_x + \frac{A_x}{A}\rho u^2 = 0 \tag{6.13b}$$

$$E_t + (u(E + p))_x + \frac{A_x}{A}u(E + p) = 0 \tag{6.13c}$$

where E is the energy, $E = \frac{p}{\gamma - 1} + \frac{1}{2}\rho u^2, A(x) = \pi R(x)^2$. The geometry of nozzle is shown in Figure 6.9. $R(x)$ is the radius of the nozzle's cross section. Its expression is as

follows.

$$R = \begin{cases} 0.5, x < -0.4 \\ -24.5571(x+0.4)^4 + 26.1942(x+0.4)^3 - 7.8586(x+0.4)^2 + 0.5, -0.4 \le x \le 0 \\ -0.0265(x+0.4)^4 + 0.0991(x+0.4)^3 - 0.0934(x+0.4)^2 + 0.0340(x+0.4) \\ \quad + 0.2861, 0 < x \le 1.6 \\ 0.3484, x > 1.6 \end{cases}$$

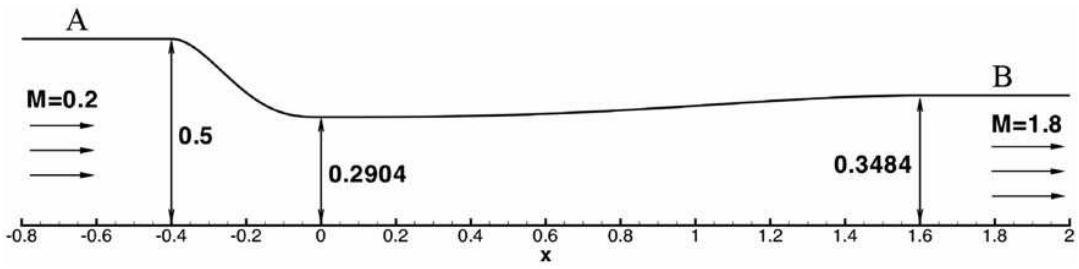

Fig. 6.9. supersonic nozzle geometry.

At $t = 0$, an entropy wave pulse (density perturbation) in the form given below:

$$\rho' = 0.001 \exp\left(-(\ln 2)\left(\frac{x - x_0 - \bar{u}t}{3\Delta/(q_0+1)}\right)^2\right) \tag{6.14a}$$

$$p' = 0 \tag{6.14b}$$

$$u' = 0 \tag{6.14c}$$

where

$$\Delta = \text{mesh spacing} \tag{6.15a}$$

$$x_0 = -1.2 \tag{6.15b}$$

$$\bar{u} = 0.2 \tag{6.15c}$$

$$q_0 = \begin{cases} q, & \text{if we use the DG-}P^q\text{ scheme.} \\ 0, & \text{if we use any FD schemes.} \end{cases} \tag{6.15d}$$

enters the computational domain on the left at $x = x_0$. The entropy pulse is convected downstream by the mean flow. As the entropy wave moves downstream through the nozzle, sound is generated. Firstly, we take the analytic mean flow as the initial value and obtain a numerical mean flow through repeated iterations as shown in Figures 6.11

and 6.13. Then we add the entropy pulse to get the results. In order to observe the results, we first fix the observation points, compute the pressure at station A located at $x = -1.0$ and at station B located at $x = 2.2$ until the entropy wave pulse exits the computational domain on the right. We use DG-P^1 and DG-P^2, respectively. The time step is set as:

$$\Delta t = \frac{1}{30} \frac{\Delta}{\max\limits_j (|u_j| + c_j)} \tag{6.16}$$

where u_j and c_j are computed from $\bar{\rho}_j, \bar{m}_j$ and $\bar{E}_j$. Characteristic boundary conditions are used in this example. Figures 6.12 and 6.14 show their time history results.

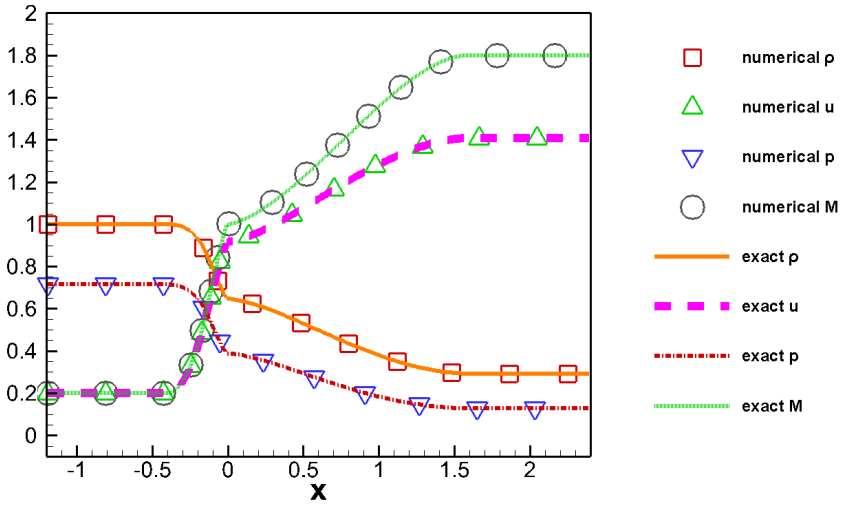

Fig. 6.10. Numerical and analytical average flow. The Mach number $M = \frac{u}{\sqrt{\gamma p/\rho}}$ is also presented. DG-P^2, $N = 300$ are used.

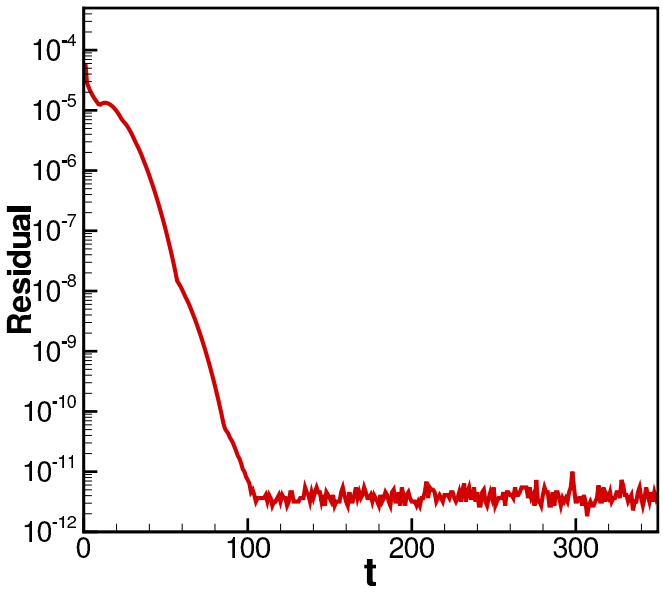

Fig. 6.11. The residual of ρ. DG-P^1, $N = 450$.

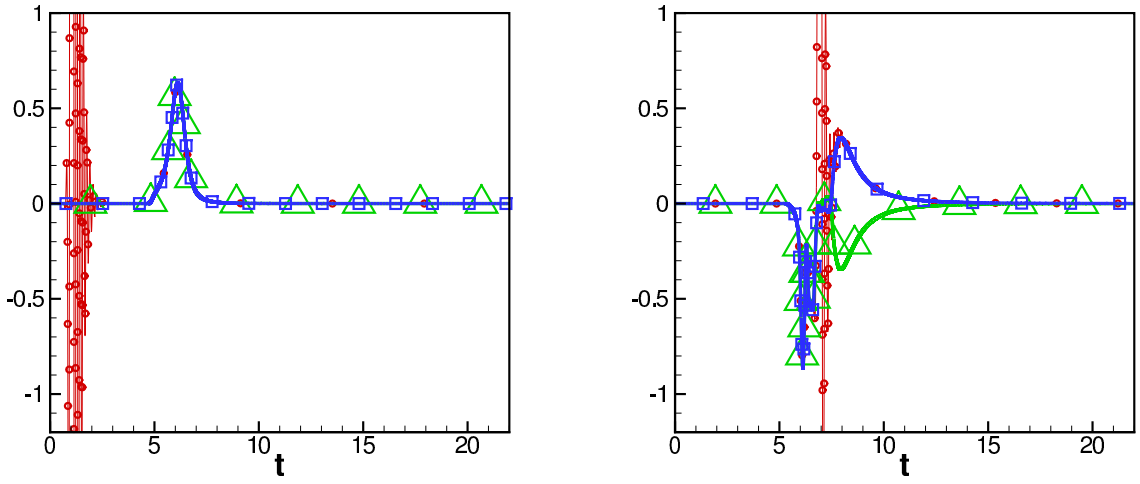

Fig. 6.12. Left: Time history for the upstream observation point A. Small circle, delta and square symbols stand for $(\rho - \bar{\rho})a_u^2 \times 10^5$, $-(u - \bar{u})\rho_u a_u \times 10^5$, and $(p - \bar{p}) \times 10^5$ respectively. Right: Time history for the downstream observation point B. Small circle, delta and square symbols stand for $(\rho - \bar{\rho})a_d^2 \times 10^5$, $(u - \bar{u})\rho_d a_d \times 10^5$, and $(p - \bar{p}) \times 10^5$ respectively. ρ_u, ρ_d, a_u, a_d are the mean density and sound velocity of the upstream and the downstream, respectively. DG-P^1, $N = 450$.

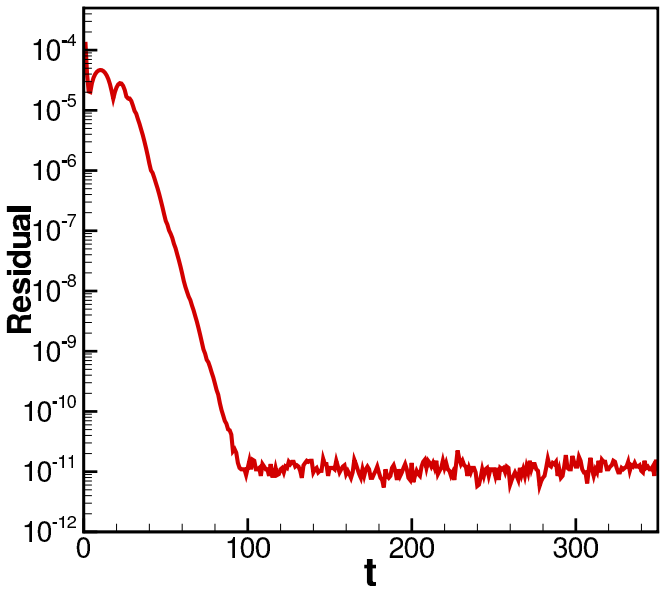

Fig. 6.13. The residual of ρ. DG-P^2, N=300.

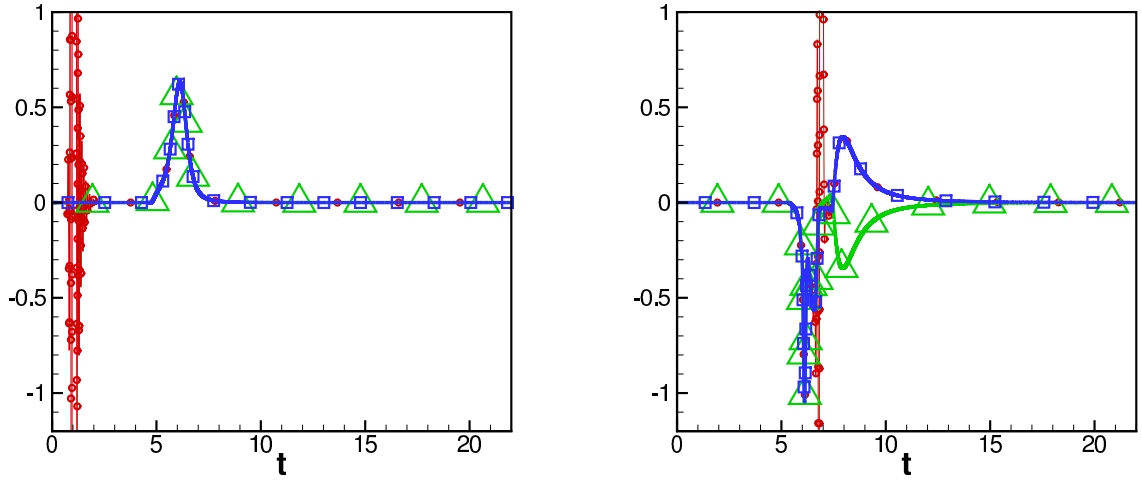

Fig. 6.14. Left: Time history for the upstream observation point A. Small circle, delta and square symbols stand for $(\rho-\bar{\rho})a_u^2\times 10^5$, $-(u-\bar{u})\rho_u a_u\times 10^5$, and $(p-\bar{p})\times 10^5$ respectively. Right: Time history for the downstream observation point B. Small circle, delta and square symbols stand for $(\rho-\bar{\rho})a_d^2\times 10^5$, $(u-\bar{u})\rho_d a_d\times 10^5$, and $(p-\bar{p})\times 10^5$ respectively. DG-P^2, $N=300$.

Then, we change the initial pulse of ρ to:

$$\rho^{'}=0.001\exp\left(-(\ln 2)\left(\frac{x-x_0+9\Delta/(q_0+1)-\bar{u}t}{3\Delta/(q_0+1)}\right)^2\right)$$

and fix the observation time and observe the distribution of the physical quantities in space. The results are shown in Figures 6.15 and 6.16, which are in good agreement with those of the DRP-ASD scheme by Tam and Parrish [32, 33], reproduced in Figure 6.17, showing that the DG schemes are compatible with the DRP-ASD scheme for the nozzle flow in simulating such non-linear and small amplitude acoustic wave propagation problem well.

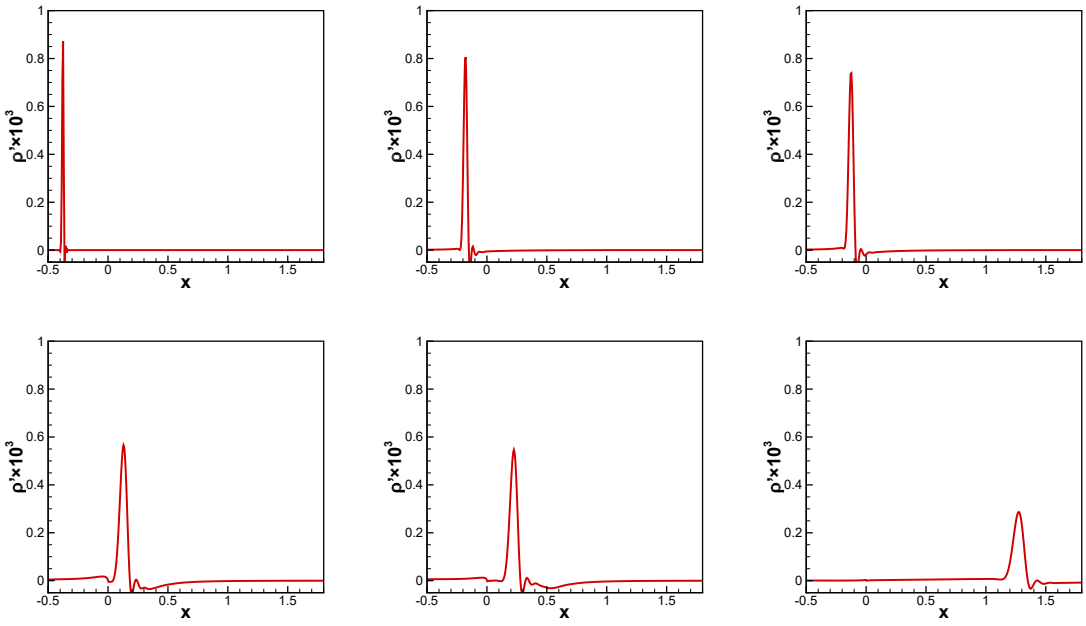

Fig. 6.15. Instantaneous density distributions inside the supersonic nozzle as the entropy pulse is convected downstream. DG-P^2, $N = 600$. $t = 4.2, 4.9, 5.0, 5.3, 5.4, 6.3$. Subgraphs are arranged in the order from left to right, then from top to bottom.

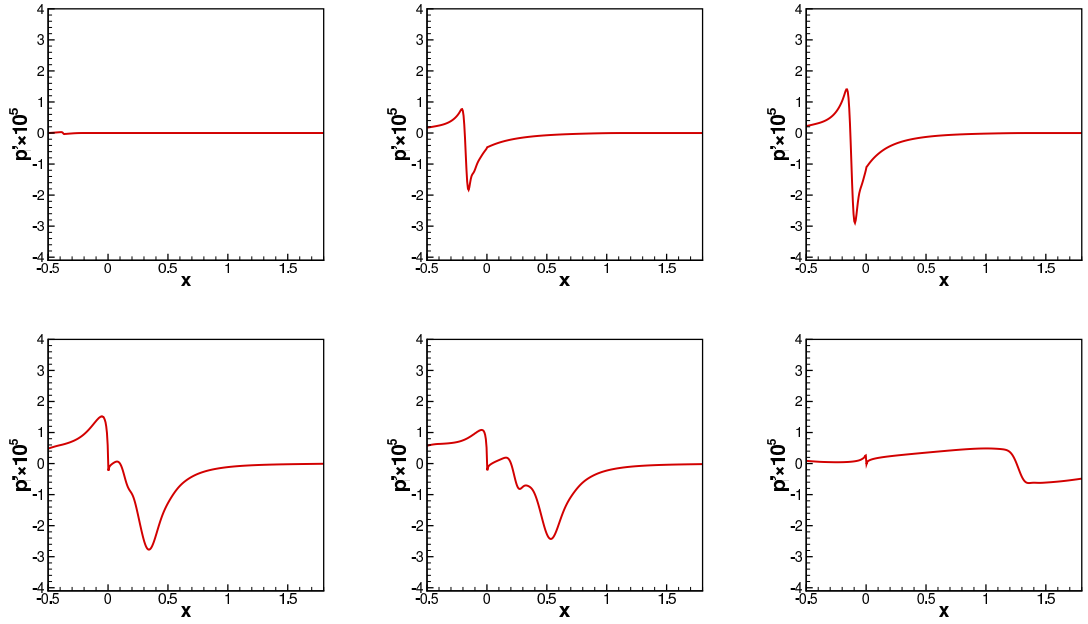

Fig. 6.16. Instantaneous pressure distributions inside the supersonic nozzle as the entropy pulse is convected downstream. DG-P^2, $N = 600$. $t = 4.2, 4.9, 5.0, 5.3, 5.4, 6.3$. Subgraphs are arranged in the order from left to right, then from top to bottom.

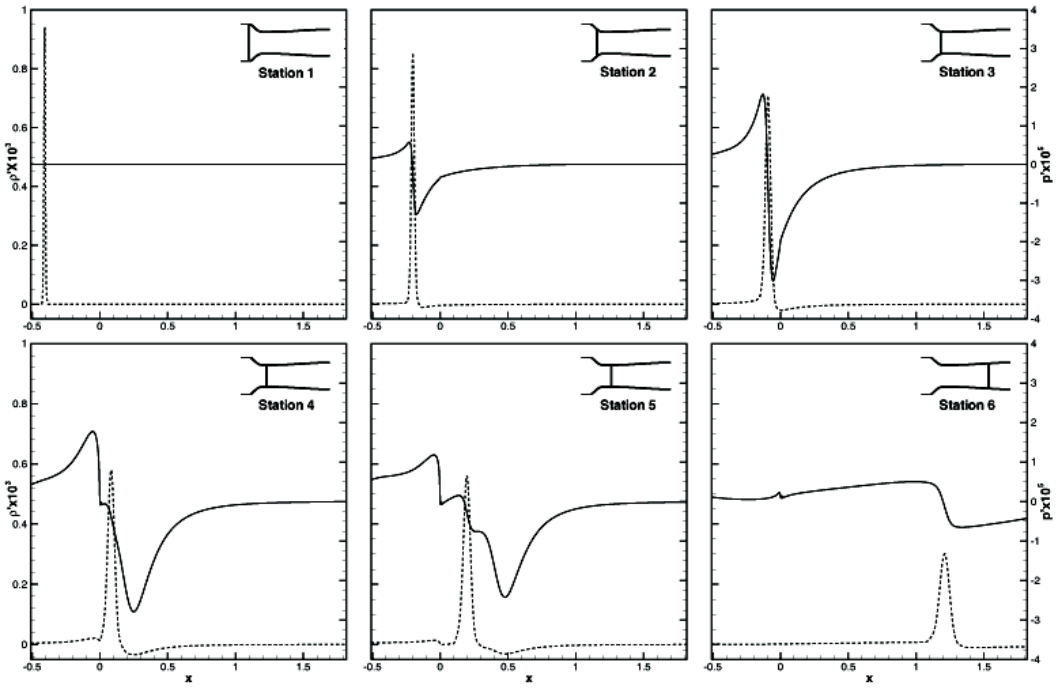

Fig. 6.17. Instantaneous density and pressure distributions inside the supersonic nozzle as the entropy pulse is convected downstream. Results in [32].

Example 6.7. Tam and Parrish also presented a subsonic-subsonic nozzle in [32],

where:

$$D(x) = \begin{cases} 1, & x \le -0.59 \\ 8.343301(x+0.59)^3 - 6.011463(x+0.59)^2 + 1, & -0.59 < x \le -0.25 \\ -0.293408(x+0.59)^3 + 2.797980(x+0.59)^2 - 2.995210(x+0.59) & \\ \quad + 1.339457, & -0.25 < x \le 0 \\ -5.310065(x+0.59)^3 + 12.640609(x+0.59)^2 - 9.370618(x+0.59) & \\ \quad + 2.705044, & 0 < x \le 0.407 \\ 0.665, & x \ge 0.407 \end{cases}$$

and $R(x) = D(x)/2$. The geometry of the nozzle and the mean flow are presented in

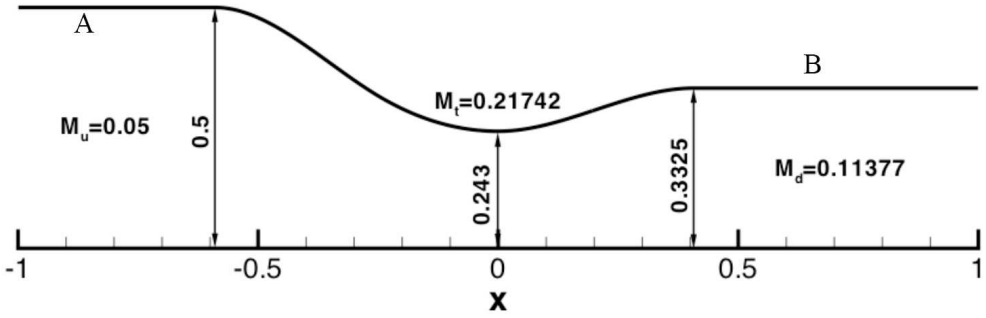

Fig. 6.18. subsonic nozzle geometry.

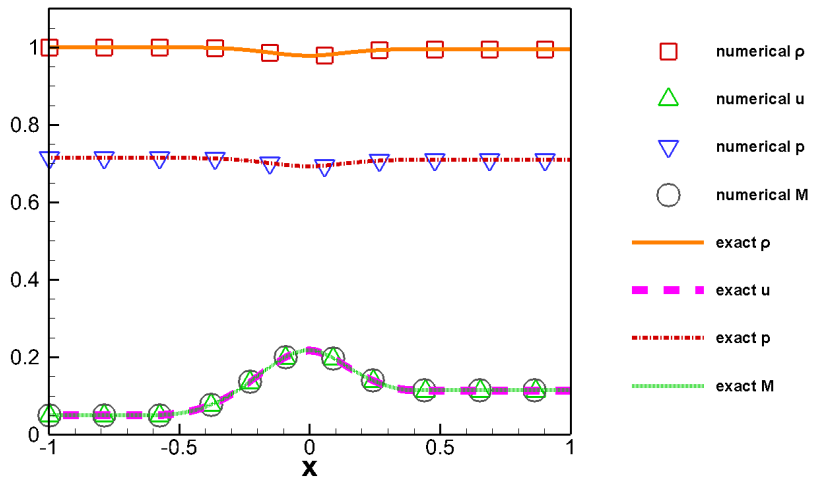

Fig. 6.19. Numerical and analytical average flow. The Mach number $M = \frac{u}{\sqrt{\gamma p/\rho}}$ is also presented. DG-P^3, $N = 1000$ are used.

Figures 6.18 and 6.19 respectively. At $t = 0$, an entropy wave pulse (density perturbation) in the form given below,

$$\rho' = \exp\left(-\ln 2\left(\frac{x - x_0 + 9\Delta/(q_0+1) - \bar{u}t}{3\Delta/(q_0+1)}\right)^2\right) \tag{6.17a}$$

$$p^{'} = 0 \tag{6.17b}$$

$$u^{'} = 0 \tag{6.17c}$$

where

$$\Delta = \text{mesh spacing} \tag{6.18a}$$

$$x_0 = -1 \tag{6.18b}$$

$$\bar{u} = 0.05 \tag{6.18c}$$

$$q_0 = \begin{cases} q, & \text{if we use the DG-}P^q\text{ scheme.} \\ 0, & \text{if we use any FD schemes.} \end{cases} \tag{6.18d}$$

enters the computational domain on the left at $x = x_0$. The time step settings in this example are consistent with those in Example 6.6.

Although we use the original Euler equation while [32] uses its linearized version, we still get consistent results. It is worth noting that for boundary conditions, [32] uses perfectly matched layer (PML) boundary conditions while we only use simple characteristic boundary conditions. This example demonstrates that the DG scheme performs well in simulating indirect combustion noise generation in ducted flows.

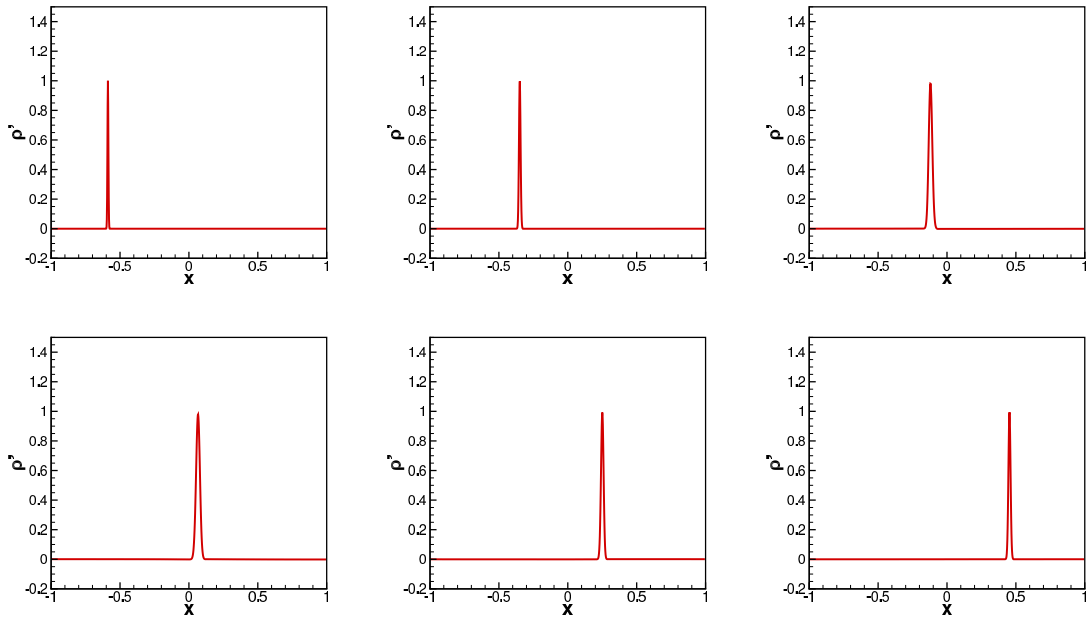

Fig. 6.20. Instantaneous pressure distributions inside the subsonic nozzle as the entropy pulse is convected downstream. DG-P^3, $h = 2/1000$. $t = 8.5, 12.5, 14.3, 15.2, 16.3, 18$. Subgraphs are arranged in the order from left to right, then from top to bottom.

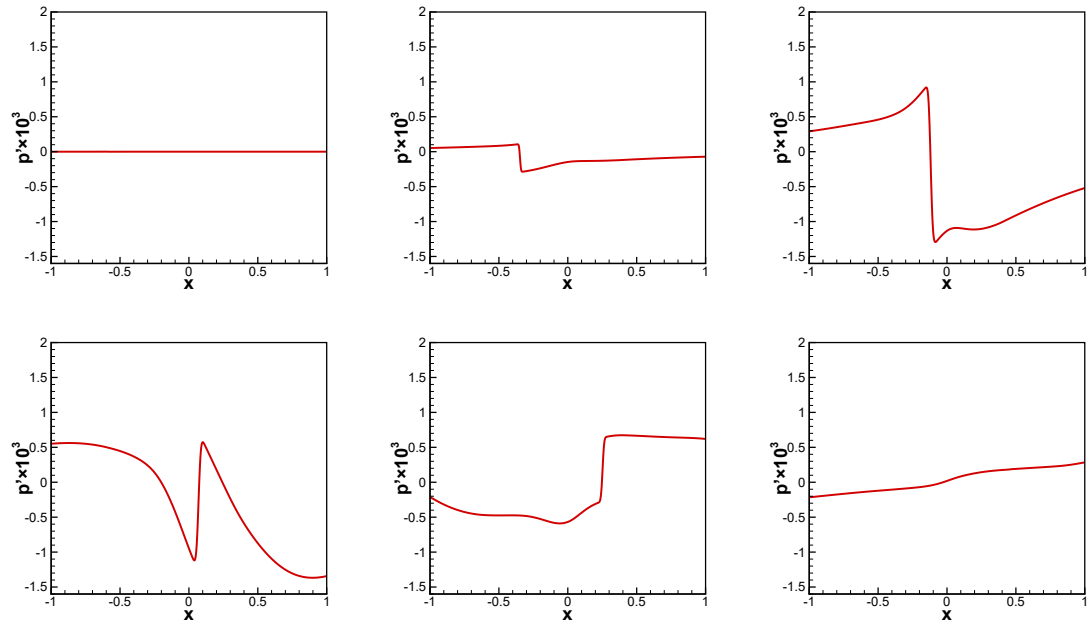

Fig. 6.21. Instantaneous pressure distributions inside the subsonic nozzle as the entropy pulse is convected downstream. DG-P^3, $h = 2/1000$. $t = 8.5, 12.5, 14.3, 15.2, 16.3, 18$. Subgraphs are arranged in the order from left to right, then from top to bottom.

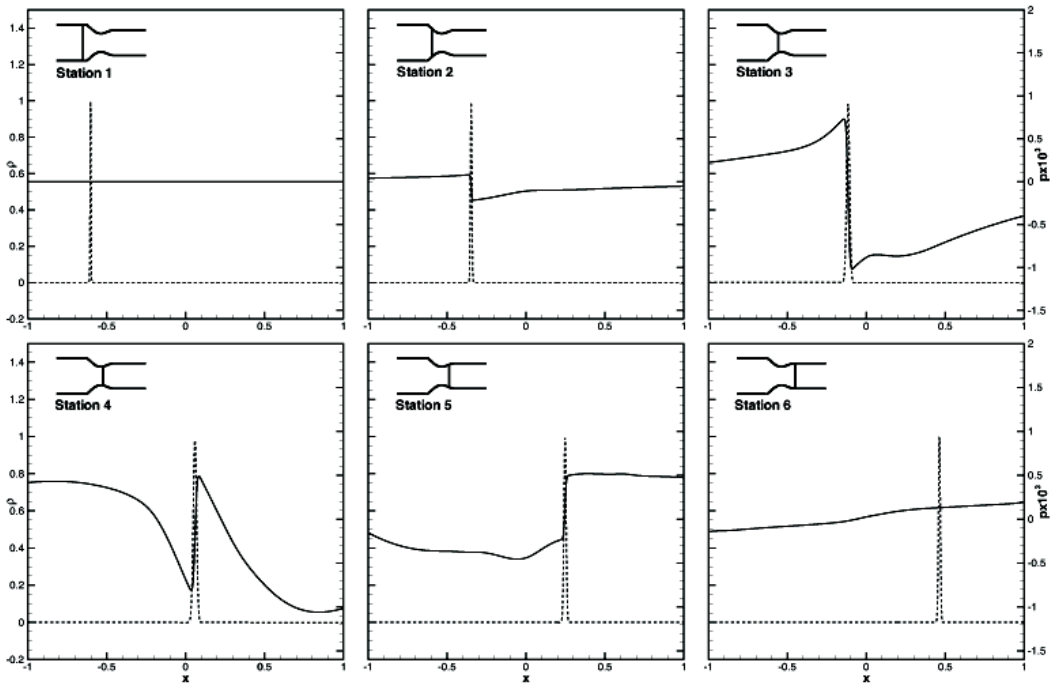

Fig. 6.22. Instantaneous density and pressure distributions inside the subsonic nozzle as the entropy pulse is convected downstream. The results of the DRP-ASD scheme in [32].

7 Conclusion

In this paper, we discuss the propagation properties of the DG schemes in detail and compare them with several finite difference schemes including the DRP scheme. We find that the propagation properties of DG-P^q scheme is complex: the initial wave can be divided into $q+1$ waves propagating according to different properties respectively. In the long wave range, only one of them is close to the propagation properties of the exact solution, which is called the physical wave. Other waveforms have very disorderly propagation properties and strong dissipation. They are called the virtual waves. Nevertheless, the DG schemes still have good dispersion and dissipation properties, and these properties improve with the increase of order of the scheme. We also discussed the DG schemes with upwind-biased flux and found that their dispersion properties depend on both θ and polynomial degree q. For many test problems, the DG-P^5 (a 7-point scheme) and the optimized 7-point DRP scheme, have comparable dispersion properties. A series

of numerical examples verify our theoretical analysis. We find that the DG schemes are comparable in resolution with the DRP scheme with the same stencil for many standard test cases, including for the nozzle flow problems.

Since the DG schemes have many advantages than finite difference schemes on non-uniform meshes and general unstructured meshes, the DG schemes have a good potential in CAA applications. Moreover, the "block finite difference" schemes can be derived from the standard DG schemes as shown in this paper, but they are more general than DG schemes. More study will be performed to identify good "block finite difference" schemes especially for CAA problems.

For future research, we will implement DG schemes on more complex problems, including multi-dimensional problems and problems with complex geometries, to assess their resolution properties for CAA applications, especially on their resolution property of short wave components. Study of DG-based finite difference schemes to general wave propagation problems, following the earlier work of Fernando and Hu [12], would also be worth pursuing.

8 Acknowledgement

We would like to thank Professor Christopher Tam for his very helpful comments, which have led to an improvement of this paper.

A Proof for Lemma 4.2

First, we write $u_h(k,x,t)$ in the algebraic form of complex functions:

$$\begin{aligned} u_h(k,x,t)|_{I_j} &= \sum_{m=0}^{q} u_m^j(t)\varphi_m^j(x) = \sum_{m=0}^{q} u_{mr}^j(t)\varphi_m^j(x) + i\sum_{m=0}^{q} u_{mi}^j(t)\varphi_m^j(x) \\ &= u_{hr}(k,x,t) + iu_{hi}(k,x,t) \end{aligned} \tag{A.1}$$

where $u_{mr}^j(t)$, $u_{mi}^j(t)$, $u_{hr}(k,x,t)$, $u_{hi}(k,x,t) \in \boldsymbol{R}$. According to the linearity of the L^2 projection operator and the DG scheme, it is easy to verify that $u_{hr}(k,x,t)$ and $u_{hi}(k,x,t)$

are the corresponding DG solutions of the follow equations:

$$\begin{cases} u_t + u_x = 0 \\ \\ u(x,0) = \cos kx, \end{cases} \qquad \begin{cases} u_t + u_x = 0 \\ \\ u(x,0) = \sin kx \end{cases}$$

It is obvious that $|k| > k_0 > 0$. We assume that $M = \left[\frac{|k|h}{2\pi}\right] + 1$. Suppose that $k \in [k_1, k_2]$, and k_1, k_2 are given by:

$$\frac{2\pi M}{k_1 h} = \left[\frac{2\pi M}{|k|h}\right] + 1, \quad \frac{2\pi M}{k_2 h} = \left[\frac{2\pi M}{|k|h}\right] \qquad \text{when}(k > 0) \tag{A.2}$$

or:

$$\frac{2\pi M}{k_1 h} = -\left[\frac{2\pi M}{|k|h}\right], \quad \frac{2\pi M}{k_2 h} = -\left[\frac{2\pi M}{|k|h}\right] - 1 \qquad \text{when}(k < 0) \tag{A.3}$$

It is easy to verify that $u_h(k_1, x, t)$, $u_{hr}(k_1, x, t)$, $u_{hi}(k_1, x, t)$ are all periodic functions with a period of $2\pi M/|k_1|$ for x. Let us consider the value of $u_{hr}(k_1, x, t)$ over a period $[0, 2\pi M/|k_1|]$. In [28], it is pointed out that u_{hr} satisfies the following L^2 stability in a period:

$$||u_{hr}(k_1, x, t)||_{L^2[0,2\pi M/|k_1|]} \leq ||u_{hr}(k_1, x, 0)||_{L^2[0,2\pi M/|k_1|]} \tag{A.4}$$

Through the properties of inequalities we get:

$$\frac{2\pi M}{|k_{1,2}|h} \leq \frac{2\pi M}{|k|h} + 1 \leq \frac{2\pi}{|k|h} + 2 < \frac{2\pi}{k_0 h} + 2 \tag{A.5}$$

We expand the expression of $||u_{hr}(k_1, x, t)||_{L^2[0,2\pi M/|k_1|]}$ and use the properties of Legendre polynomials to obtain:

$$\begin{aligned} &||u_{hr}(k_1, x, t)||_{L^2[0,2\pi M/|k_1|]} \\ =&\sqrt{\sum_{p=1}^{N} \int_{I_p} \left(\sum_{m=0}^{q} u_{mr}^p(t) \varphi_m^p(x) \right)^2 dx} \\ =&\sqrt{\sum_{p=1}^{N} \left(\sum_{m=0}^{q} u_{mr}^p(t)^2 \int_{I_p} (\varphi_m^p(x))^2 dx + 2 \sum_{l=0}^{q} \sum_{m=0, m\neq l}^{q} u_{lr}^p(t) u_{mr}^p(t) \int_{I_p} \varphi_l^p(x) \varphi_m^p(x) dx \right)} \\ =&\sqrt{\sum_{p=1}^{N} \sum_{m=0}^{q} \frac{h}{2m+1} (u_{mr}^p(t))^2} \\ \geq&\sqrt{\frac{h}{2s+1}} |u_{sr}^j(t)| \end{aligned} \tag{A.6}$$

where $N = 2\pi M/(|k_1|h)$, $s = 0, 1, \cdots, q$, $j = 1, 2, \cdots, N$.

On the other hand:

$$\begin{aligned}
&||u_{hr}(k_1, x, 0)||_{L^2[0,2\pi M/|k_1|]} \\
=&\sqrt{\sum_{p=1}^{N}\sum_{m=0}^{q}\frac{h}{2m+1}(u_{mr}^{p}(0))^2} \\
=&\sqrt{\sum_{p=1}^{N}\sum_{m=0}^{q}\frac{h}{2m+1}\left(\frac{2m+1}{2}\right)^2\left(\int_{-1}^{1}\varphi_m(\xi)\cos k_1\left(x_p+\frac{h\xi}{2}\right)d\xi\right)^2} \\
\leq&\sqrt{\sum_{p=1}^{N}\sum_{m=0}^{q}\frac{(2m+1)h}{4}\int_{-1}^{1}\varphi_m^2(\xi)d\xi\int_{-1}^{1}\cos^2 k_1\left(x_p+\frac{h\xi}{2}\right)d\xi} \\
=&\sqrt{\sum_{p=1}^{N}\sum_{m=0}^{q}\frac{h}{2}\left(1+\frac{\sin k_1 h}{k_1 h}\cos\left((2p-1)k_1 h\right)\right)} \\
\leq&\sqrt{\frac{2(q+1)\pi M}{|k_1|}} < \sqrt{\frac{2(q+1)(k_0 h+\pi)}{k_0}}
\end{aligned} \tag{A.7}$$

Combining (A.4,A.6,A.7), we get

$$|u_{sr}^{j}(t)| < \sqrt{\frac{2(2s+1)(q+1)(k_0 h+\pi)}{k_0 h}} \tag{A.8}$$

and

$$\begin{aligned}
|u_{hr}(k_1, x, t)|_{I_j}| = \left|\sum_{s=0}^{q}u_{sr}^{j}(t)\varphi_s^j(x)\right| &< \sum_{s=0}^{q}\sqrt{\frac{2(2s+1)(q+1)(k_0 h+\pi)}{k_0 h}}||\varphi_s^j(x)||_{L^\infty(I_j)} \\
&<(q+1)\sqrt{\frac{2(2q+1)(q+1)(k_0 h+\pi)}{k_0 h}}
\end{aligned} \tag{A.9}$$

The last inequality holds because $|\varphi_s^j(x)| \leq 1$. Using the same method, we can get the same results about u_{hi} and $u_h(k_2, x, t)$. According to the continuity of $u_h(k, x, t)$ for k we can get the conclusion:

$$|u_h(k, x, t)| < 2(q+1)\sqrt{\frac{(2q+1)(q+1)(k_0 h+\pi)}{k_0 h}} \tag{A.10}$$

Then, we return u_{hr} to DG scheme to get:

$$\begin{aligned}|(u_{sr}^j)_t| =& \left|\frac{2s+1}{h}\left(\sum_{m=0}^{q} u_{mr}^j \int_{-1}^{1} \varphi_m(\xi)\varphi_s^{'}(\xi)d\xi - \sum_{m=0}^{q} u_{mr}^j + \sum_{m=0}^{q} u_{mr}^{j-1}(-1)^s\right)\right| \\ <& \frac{2s+1}{h}\left[\sum_{m=0}^{q}\sqrt{\frac{2(2m+1)(q+1)(k_0h+\pi)}{k_0h}}\left(2+\sqrt{\frac{2}{2m+1}}||\varphi_s^{'}(\xi)||_{L^2(-1,1)}\right)\right] \\ <& \frac{(2s+1)(q+1)}{h}\sqrt{\frac{2(q+1)(k_0h+\pi)}{k_0h}}(2\sqrt{2q+1}+\sqrt{2}M_0)\end{aligned} \tag{A.11}$$

Using the same method of estimating u_h, we can get:

$$\left|\frac{\partial u_h}{\partial t}(k,x,t)\right| < \frac{2(2q+1)(q+1)^2}{h}\sqrt{\frac{(q+1)(k_0h+\pi)}{k_0h}}(2\sqrt{2q+1}+\sqrt{2}M_0) \tag{A.12}$$

B Proof for Theorem 4.1

First, let us denote the bounds as follows:

$$M_1 = 2(q+1)\sqrt{\frac{(2q+1)(q+1)(k_0h+\pi)}{k_0h}} \tag{B.1}$$

$$M_2 = \frac{2(2q+1)(q+1)^2}{h}\sqrt{\frac{(q+1)(k_0h+\pi)}{k_0h}}(2\sqrt{2q+1}+\sqrt{2}M_0) \tag{B.2}$$

Since when $k > k_0$, $\hat{f}(k)u_h(k,x,t) < M_1|\hat{f}(k)| \in L^1(-\infty,\infty)$, the first conclusion of Theorem 4.1 can be easy proved by Weierstrass discriminant. It is easy to see that $\tilde{u}_h \in V_h^q$. In order for the second conclusion to be valid, we only need to prove the following two points:

- Initial condition:

$$\tilde{u}_h(x,0) = \int_{-\infty}^{\infty} \hat{f}(k)u_h(k,x,0)dk = P_{L^2}(f(x)) \tag{B.3}$$

- For any $v_h \in V_h^q$, the DG formula holds:

$$\int_{I_j}(\tilde{u}_h)_t v_h dx = \int_{I_j}\tilde{u}_h(v_h)_x dx - (\tilde{u}_h)_{j+1/2}^{-}(v_h)_{j+1/2}^{-} + (\tilde{u}_h)_{j-1/2}^{-}(v_h)_{j-1/2}^{+} \tag{B.4}$$

For $v_h \in V_h^q$ and $x \in I_j$, we let

$$F(k,x) = \hat{f}(k)(u_h(k,x,0) - e^{ikx})v_h(x) \tag{B.5}$$

$$G(k,x,t) = \hat{f}(k)\frac{\partial u_h}{\partial t}(k,x,t)v_h(x) \tag{B.6}$$

$$H(k,x,t) = \hat{f}(k)u_h(k,x,t)(v_h)_x \tag{B.7}$$

$$I(k,x,t) = \hat{f}(k)u_h(k,x,t) \tag{B.8}$$

The following inequalities hold when $k > k_0$:

$$|F(k,x)| \leq (M_1+1)|\hat{f}(k)|||v_h||_{L^\infty(I_j)} \tag{B.9}$$

$$|G(k,x,t)| \leq M_2|\hat{f}(k)|||v_h||_{L^\infty(I_j)} \tag{B.10}$$

$$|H(k,x,t)| \leq M_1|\hat{f}(k)|||(v_h)_x||_{L^\infty(I_j)} \tag{B.11}$$

$$|I(k,x,t)| \leq M_1|\hat{f}(k)| \tag{B.12}$$

Noting that $(M_1+1)|\hat{f}(k)|||v_h||_{L^\infty(I_j)} \in L^1(-\infty,\infty)$, we know that the integral $\int_{-\infty}^{\infty} F(k,x)dk$ converges uniformly on I_j according to Weierstrass discriminant. From Lemma 4.1 we know $F(k,x) \in C(-\infty,\infty) \times I_j$. Then we get:

$$\int_{I_j}\int_{-\infty}^{\infty} F(k,x)dkdx = \int_{-\infty}^{\infty}\int_{I_j} F(k,x)dxdk \tag{B.13}$$

For $G(k,x,t)$, $H(k,x,t)$, $I(k,x,t)$, there are similar results.

For all $v_h \in V_h^q$, the following formula holds:

$$\begin{aligned}
&\int_{I_j}\left(\int_{-\infty}^{\infty}\hat{f}(k)u_h(k,x,0)dk - f(x)\right)v_h(x)dx \\
=&\int_{I_j}\left(\int_{-\infty}^{\infty}\hat{f}(k)(u_h(k,x,0) - e^{ikx})dk\right)v_h(x)dx \\
=&\int_{I_j}\left(\int_{-\infty}^{\infty}\hat{f}(k)(u_h(k,x,0) - e^{ikx})v_h(x)dk\right)dx \\
=&\int_{-\infty}^{\infty}\left(\int_{I_j}\hat{f}(k)(u_h(k,x,0) - e^{ikx})v_h(x)dx\right)dk \\
=&\int_{-\infty}^{\infty}\hat{f}(k)\left(\int_{I_j}(u_h(k,x,0) - e^{ikx})v_h(x)dx\right)dk \\
=&0
\end{aligned} \tag{B.14}$$

The last equality is established because $u_h(k,x,0) = P_{L^2}(e^{ikx})$. Therefore, (B.3) has been proved.

In the same way, we can get the following facts:

$$\int_{I_j} (\tilde{u}_h)_t v_h dx = \int_{-\infty}^{\infty} \hat{f}(k) \int_{I_j} (u_h)_t v_h dx dk \tag{B.15}$$

$$\int_{I_j} \tilde{u}_h (v_h)_x dx = \int_{-\infty}^{\infty} \hat{f}(k) \int_{I_j} u_h (v_h)_x dx dk \tag{B.16}$$

Then we construct Lagrangian basis functions $\phi_0^j, \phi_1^j, \cdots, \phi_q^j$ by taking $q+1$ different points $x_0^j, x_1^j, \cdots, x_q^j$ in I_j, and write u_h in the form of Lagrangian basis as follows:

$$u_h(k,x,t) = \sum_{m=0}^{q} u_h(k, x_m^j, t)\phi_m^j(x) \tag{B.17}$$

For any given $k^{'} \in [k_0, +\infty)$, and $\epsilon > 0$, there exists a small quantity δ, such that:

$$\begin{aligned} &|u_h(k,x,t) - u_h(k, x_{j+1/2}^-, t)| \\ =&\left| \sum_{m=0}^{q} u_h(k, x_m^j, t)(\phi_m^j(x) - \phi_m^j(x_{j+1/2}^-)) \right| \\ <&M_1(q+1) \max_{m=0,1,\cdots,q} |\phi_m^j(x) - \phi_m^j(x_{j+1/2}^-)| \\ <&M_1(q+1)\epsilon \end{aligned} \tag{B.18}$$

holds for all $k \in [k_0, k^{'}]$ and $k \in [-k^{'}, -k_0]$ and $x \in (x_{j+1/2} - \delta, x_{j+1/2})$. Therefore,

$$\lim_{x \to x_{j+1/2}^-} u_h(k,x,t) = u_h(k, x_{j+1/2}^-, t) \tag{B.19}$$

holds for $k \in [k_0, k^{'}]$ and $k \in [-k^{'}, -k_0]$ uniformly. In addition, integral $\int_{-\infty}^{\infty} \hat{f}(k) u_h(k,x,t) dk$ is uniformly convergent on I_j. So we can get:

$$\begin{aligned}
&(\tilde{u}_h)(x^-_{j+1/2})(v_h)^-_{j+1/2} \\
=&\lim_{x \to x^-_{j+1/2}} \int_{-\infty}^{-k_0} \hat{f}(k) u_h(k,x,t) dk (v_h)^-_{j+1/2} + \lim_{x \to x^-_{j+1/2}} \int_{-k_0}^{k_0} \hat{f}(k) u_h(k,x,t) dk (v_h)^-_{j+1/2} \\
&+ \lim_{x \to x^-_{j+1/2}} \int_{k_0}^{\infty} \hat{f}(k) u_h(k,x,t) dk (v_h)^-_{j+1/2} \\
=&\int_{-\infty}^{-k_0} \hat{f}(k) u_h(k, x^-_{j+1/2}, t)(v_h)^-_{j+1/2} dk + \int_{-k_0}^{k_0} \hat{f}(k) u_h(k, x^-_{j+1/2}, t)(v_h)^-_{j+1/2} dk \\
&+ \int_{k_0}^{\infty} \hat{f}(k) u_h(k, x^-_{j+1/2}, t)(v_h)^-_{j+1/2} dk \\
=&\int_{-\infty}^{\infty} \hat{f}(k) u_h(k, x^-_{j+1/2}, t)(v_h)^-_{j+1/2} dk
\end{aligned} \tag{B.20}$$

Similarly,

$$(\tilde{u}_h)(x^-_{j-1/2})(v_h)^+_{j-1/2} = \int_{-\infty}^{\infty} \hat{f}(k) u_h(k, x^-_{j-1/2}, t)(v_h)^+_{j-1/2} dk \tag{B.21}$$

Combining (B.15), (B.16), (B.20) and (B.21), we can draw the following conclusion:

$$\begin{aligned}
&\int_{I_j} (\tilde{u}_h)_t v_h dx - \int_{I_j} \tilde{u}_h (v_h)_x dx + (\tilde{u}_h)^-_{j+1/2} (v_h)^-_{j+1/2} - (\tilde{u}_h)^-_{j-1/2} (v_h)^+_{j-1/2} \\
=&\int_{-\infty}^{\infty} \hat{f}(k) \left(\int_{I_j} (u_h)_t v_h dx - \int_{I_j} u_h (v_h)_x dx + (u_h)^-_{j+1/2} (v_h)^-_{j+1/2} - (u_h)^-_{j-1/2} (v_h)^+_{j-1/2} \right) dk \\
=&0
\end{aligned} \tag{B.22}$$

By this time, we have proved Theorem 4.1.

References

[1] M. Ainsworth. Dispersive and dissipative behaviour of high order discontinuous Galerkin finite element methods. *Journal of Computational Physics*, 198(1):106–130, 2004.

[2] G. Ashcroft and X. Zhang. Optimized prefactored compact schemes. *Journal of Computational Physics*, 190(2):459–477, 2003.

[3] H.L. Atkins. Continued development of the discontinuous Galerkin method for computational aeroacoustic applications. In *3rd AIAA/CEAS Aeroacoustics Conference*, page 1581, 1997. https://doi.org/10.2514/6.1997-1581

[4] H.L. Atkins and C.-W. Shu. Quadrature-free implementation of the discontinuous Galerkin method for hyperbolic equations. *AIAA Journal*, 36(5):775–782, 1998.

[5] C. Bogey and C. Bailly. A family of low dispersive and low dissipative explicit schemes for flow and noise computations. *Journal of Computational Physics*, 194(1):194–214, 2004.

[6] M.H. Carpenter, D. Gottlieb, and S. Abarbanel. The stability of numerical boundary treatments for compact high-order finite-difference schemes. *Journal of Computational Physics*, 108(2):272–295, 1993.

[7] B. Cockburn, S. Hou, and C.-W. Shu. The Runge-Kutta local projection discontinuous Galerkin finite element method for conservation laws. iv. the multidimensional case. *Mathematics of Computation*, 54(190):545–581, 1990.

[8] B. Cockburn, S.-Y. Lin, and C.-W. Shu. TVB Runge-Kutta local projection discontinuous Galerkin finite element method for conservation laws iii: one-dimensional systems. *Journal of Computational Physics*, 84(1):90–113, 1989.

[9] B. Cockburn, C.-W. Shu. TVB Runge-Kutta local projection discontinuous Galerkin finite element method for conservation laws. II. General framework. *Mathematics of Computation*, 52(186): 411-435, 1989.

[10] B. Cockburn and C.-W. Shu. The Runge-Kutta local projection-discontinuous-Galerkin finite element method for scalar conservation laws. *ESAIM: Mathematical Modelling and Numerical Analysis*, 25(3):337–361, 1991.

[11] B. Cockburn and C.-W. Shu. The Runge–Kutta discontinuous Galerkin method for conservation laws v: multidimensional systems. *Journal of Computational Physics*, 141(2):199–224, 1998.

[12] A.M. Fernando and F.Q. Hu. DGM-FD: A finite difference scheme based on the discontinuous Galerkin method applied to wave propagation. *Journal of Computational Physics*, 230(12):4871–4898, 2011.

[13] L. Gascón and J.M. Corberán. Construction of second-order TVD schemes for nonhomogeneous hyperbolic conservation laws. *Journal of Computational Physics*, 172(1):261–297, 2001.

[14] W. Guo, X. Zhong, and J.-M. Qiu. Superconvergence of discontinuous Galerkin and local discontinuous Galerkin methods: eigen-structure analysis based on Fourier approach. *Journal of Computational Physics*, 235:458–485, 2013.

[15] B. Gustafsson, H.-O. Kreiss, and J. Oliger. *Time Dependent Problems and Difference Methods*, volume 24. John Wiley & Sons, 1995.

[16] T. Hagstrom, J. Goodrich, I. Nazarov, and C. Dodson. High-order methods and boundary conditions for simulating subsonic flows. In *11th AIAA/CEAS Aeroacoustics Conference*, page 2869, 2005. DOI: 10.2514/6.2005-2869

[17] J.C. Hardin, J.R. Ristorcelli, and C.K.W. Tam. ICASE/LaRC workshop on benchmark problems in computational aeroacoustics (CAA). *National Aeronautics and Space Administration*, NASA Conference Publication 3300, 1995.

[18] R. Hixon. Prefactored small-stencil compact schemes. *Journal of Computational Physics*, 165(2):522–541, 2000.

[19] F.Q. Hu and H.L. Atkins. Eigensolution analysis of the discontinuous Galerkin method with nonuniform grids: I. one space dimension. *Journal of Computational Physics*, 182(2):516–545, 2002.

[20] F.Q. Hu, M.Y. Hussaini, and P. Rasetarinera. An analysis of the discontinuous Galerkin method for wave propagation problems. *Journal of Computational Physics*, 151(2):921–946, 1999.

[21] D.S. Jones, M. Kline. Asymptotic expansion of multiple integrals and the method of stationary phase. *Journal of Mathematics and Physics*, 37(1-4): 1-28, 1958.

[22] J.W. Kim and D.J. Lee. Optimized compact finite difference schemes with maximum resolution. *AIAA Journal*, 34(5):887–893, 1996.

[23] J.W. Kim and D.J. Lee. Implementation of boundary conditions for optimized high-order compact schemes. *Journal of Computational Acoustics*, 5(02):177–191, 1997.

[24] S.K. Lele. Compact finite difference schemes with spectral-like resolution. *Journal of Computational Physics*, 103(1):16–42, 1992.

[25] X. Meng, C.-W. Shu, and B. Wu. Optimal error estimates for discontinuous Galerkin methods based on upwind-biased fluxes for linear hyperbolic equations. *Mathematics of Computation*, 85(299):1225–1261, 2016.

[26] W.H. Reed and T.R. Hill. Triangular mesh methods for the neutron transport equation. Technical report, Los Alamos Scientific Lab, N. Mex.(USA), 1973.

[27] S. Sherwin. Dispersion analysis of the continuous and discontinuous Galerkin formulations. In *Discontinuous Galerkin Methods*, pages 425–431. Springer, 2000.

[28] C.-W. Shu. Discontinuous Galerkin methods: general approach and stability. in *Numerical Solutions of Partial Differential Equations*, Advanced Courses in Mathematics CRM Barcelona, Birkhäuser, Basel, 2009, pp.149-201.

[29] C.-W. Shu and S. Osher. Efficient implementation of essentially non-oscillatory shock-capturing schemes. *Journal of Computational Physics*, 77(2):439–471, 1988.

[30] C.K.W. Tam. Supersonic jet noise. *Annual Review of Fluid Mechanics*, 27(1):17–43, 1995.

[31] C.K.W. Tam. *Computational Aeroacoustics: a Wave Number Approach*, volume 33. Cambridge University Press, 2012.

[32] C.K.W. Tam and S.A. Parrish. On the generation of indirect combustion noise. In *20th AIAA/CEAS Aeroacoustics Conference*, page 3315, 2014. https://doi.org/10.2514/6.2014-3315

[33] C.K.W. Tam and S.A. Parrish. The physical processes of indirect combustion noise generation. *International Journal of Aeroacoustics*, 17(1-2):22–35, 2018.

[34] C.K.W. Tam, S.A. Parrish, J. Xu, and B. Schuster. Indirect combustion noise of auxiliary power units. *Journal of Sound and Vibration*, 332(17):4004–4020, 2013.

[35] C.K.W. Tam and H. Shen. Direct computation of nonlinear acoustic pulses using high-order finite difference schemes. In *15th Aeroacoustics Conference*, page 4325, 1993. https://doi.org/10.2514/6.1993-4325

[36] C.K.W. Tam and J.C. Webb. Dispersion-relation-preserving finite difference schemes for computational acoustics. *Journal of Computational Physics*, 107(2):262–281, 1993.

[37] C.K.W. Tam, J.C. Webb, and Z. Dong. A study of the short wave components in computational acoustics. *Journal of Computational Acoustics*, 1(01):1–30, 1993.

[38] J.H. Wilkinson. The Algebraic Eigenvalue Problem. *Clarendon: Oxford*, 1965.

[39] M. Zhang and C.-W. Shu. An analysis of three different formulations of the discontinuous Galerkin method for diffusion equations. *Mathematical Models and Methods in Applied Sciences*, 13(03):395–413, 2003.

[40] X. Zhong and C.-W. Shu. Numerical resolution of discontinuous Galerkin methods for time dependent wave equations. *Computer Methods in Applied Mechanics and Engineering*, 200(41-44):2814–2827, 2011.

[41] J. Zhu, J. Qiu, C.-W. Shu, M. Dumbser. Runge-Kutta discontinuous Galerkin method using WENO limiters II: Unstructured meshes. *Journal of Computational Physics*, 227(9): 4330-4353, 2008,

[42] M. Zhuang and R.F. Chen. Optimized upwind dispersion-relation-preserving finite difference scheme for computational aeroacoustics. *AIAA Journal*, 36(11):2146–2148, 1998.

[43] M. Zhuang and R.F. Chen. Applications of high-order optimized upwind schemes for computational aeroacoustics. *AIAA Journal*, 40(3):443–449, 2002.